The hydrological cycle and ocean circulation of the Maritime Continent in the mid-Pliocene: results from PlioMIP2

Xin Ren[1], Daniel J. Lunt[1], Erica Hendy[1], Anna von der Heydt[2], Ayako Abe-Ouchi[3], Bette Otto-Bliesner[4], Charles J. R. Williams[1,5], Christian Stepanek[6], Chuncheng Guo[7], Deepak Chandan[8], Gerrit Lohmann[6], Julia C. Tindall[9], Linda E. Sohl[10,11], Mark A. Chandler[10,11], Masa Kageyama[12], Michiel L. J. Baatsen[2], Ning Tan[13,14], Qiong Zhang[15], Ran Feng[16], Wing-Le Chan[3], W. Richard Peltier[8], Xiangyu Li[17,18,19], Youichi Kamae[20], Zhongshi Zhang[7,18], and Alan M. Haywood[9]

[1]School of Geographical Sciences, University of Bristol, Bristol, UK
[2]Institute for Marine and Atmospheric research Utrecht (IMAU), Department of Physics, Utrecht University, Utrecht, the Netherlands
[3]Atmosphere and Ocean Research Institute, The University of Tokyo, Kashiwa, Japan
[4]Climate and Global Change Dynamics lab, National Center for Atmospheric research, USA
[5]NCAS, Department of Meteorology, University of Reading, Reading, UK
[6]Alfred-Wegener-Institut – Helmholtz-Zentrum für Polar and Meeresforschung (AWI), Bremerhaven, Germany
[7]NORCE Norwegian Research Centre, Bjerknes Centre for Climate Research, Bergen, Norway
[8]Department of Physics, University of Toronto, Toronto, Canada
[9]School of Earth and Environment, University of Leeds, Woodhouse Lane, Leeds, West Yorkshire, UK
[10]Center for Climate Systems Research at Columbia University, New York, NY, USA
[11]NASA Goddard Institute for Space Studies, New York, NY, USA)
[12]LSCE/IPSL – Laboratoire des Sciences du Climat et de l'Environnement, UMR8212, CEA-CNRS-UVSQ – CE Saclay, L'Orme des Merisiers, Gif-sur-Yvette Cedex, France
[13]Key Laboratory of Cenozoic Geology and Environment, Institute of Geology and Geophysics, Chinese Academy of Sciences, Beijing, China
[14]Laboratoire des Sciences du Climat et de l'Environnement, LSCE/IPSL, CEA-CNRS-UVSQ, Université Paris-Saclay, Gif-sur-Yvette, France
[15]Department of Physical Geography and Bolin Centre for Climate Research, Stockholm University, Stockholm, Sweden
[16]Department of Earth Sciences, College of Liberal Arts and Sciences, University of Connecticut, Storrs, USA
[17]Centre for Severe Weather and Climate and Hydro-geological HazardsWuhan, China
[18]Department of Atmospheric Science, School of Environmental Studies, China University of Geosciences, Wuhan, China
[19]Climate Change Research Center, Institute of Atmospheric Physics, Chinese Academy of Sciences, Beijing, China
[20]Faculty of Life and Environmental Sciences, University of Tsukuba, Tsukuba, Japan

Correspondence: Xin Ren (xinxin.ren@bristol.ac.uk)

Abstract. The Maritime Continent (MC) forms the western boundary of the tropical Pacific Ocean, and relatively small changes in this region can impact the climate locally and remotely. In the mid-Pliocene (from 3.264 to 3.025 million years before present), atmospheric CO_2 concentrations were ~ 400 ppm, and the subaerial Sunda and Sahul shelves made the land-sea distribution of the MC different to today. Topographic changes and elevated levels of CO_2, combined with other forcings, are therefore expected to have driven a substantial climate signal in the MC region at this time. By using the results from the Pliocene Model Intercomparison Project phase 2 (PlioMIP2) we study the mean climatic features of the MC in the mid-Pliocene and changes in Indonesian Throughflow (ITF) with respect to preindustrial. Results show a warmer and wetter mid-Pliocene

climate of the MC and lower sea surface salinity in the surrounding ocean compared with preindustrial. Furthermore, we quantify the volume transfer through the ITF; although the ITF may be expected to be hindered by the subaerial shelves, 10 out of 15 models show an increased volume transport compared with preindustrial.

In order to avoid undue influence from closely-related models that are present in the PlioMIP2 ensemble, we introduce a new metric - the multi-cluster mean (MCM), based on cluster analysis of the individual models. We study the effect that the choice of MCM versus the more traditional analysis of multi-model mean (MMM) and individual models has on the discrepancy between model results and ~~reconstructed proxy data. The~~ data. It has been found that models, which reproduce modern MC climate well, are not always good at simulating the mid-Pliocene climate anomaly of the MC. By comparing with individual models, the MMM and MCM reproduce the preindustrial sea surface temperature (SST) of the reanalysis better than most individual models, and produces less discrepancy with reconstructed sea surface temperature anomalies (SSTA) than most individual models in the MC. In addition, the clusters reveal spatial signals that are not captured by the MMM, so that the MCM provides us with a new way to explore the results from model ~~ensemble~~ ensembles that include similar models.

1 Introduction

The Maritime Continent (MC; 10°S–20°N and 90°E–150°E), which consists of more than 22,000 islands, lies in the warmest ocean region, the West Pacific Warm Pool (WPWP) ~~(Yoneyama and Zhang, 2020; RAMAGE, 1968)~~(RAMAGE, 1968; Yoneyama and Zha. The near-surface air temperature in most areas of the MC is higher than 27°C throughout the year (Li et al., 2018a). High sea surface temperature (SST) leads to substantial moisture flux into the atmosphere. High levels of moisture and energy characterize the unstable climate in this region and make it "the world's strongest atmospheric convection center" (Yoneyama and Zhang, 2020). Based on satellite data it has been established that the MC is the region that produces the largest amount of precipitation in the world (Adler et al., 2017; Yamanaka et al., 2018). A large amount of rainfall releases ~~large~~ vast quantities of latent heat ~~, that is an important driver of global atmospheric circulation,~~ into the atmosphere (1 mm/y equals to 0.08 W/m^2~~(Trenberth et al., 2009; Yamanaka et al., 2018))~~), which is an important driver of global atmospheric circulation (Trenberth et al., 2009; Yamanaka et al., 2018). According to these characteristics, the MC has been recognized as the "boiler box" of the global climate system (RAMAGE, 1968; Neale and Slingo, 2003).

The MC also impacts on the oceanic hydrological system in that it links the Pacific Ocean and the Indian Ocean via the Indonesian Throughflow (ITF), which is a key component of global ocean circulation. In general, the ITF transports warm and comparably fresh water from the Pacific Ocean into the Indian Ocean. Dramatic tectonic processes and sea level changes shaped this gateway that plays an important role in influencing ~~local climate and that of~~ climate both locally and in other regions of the world (Gordon, 2005b; Tillinger, 2011; Yoneyama and Zhang, 2020). According to the International Nusantara Stratifcation and Transport Program (INSTANT), from 2004 to 2006 (Gordon et al., 2010; Sprintall et al., 2009) the ITF transported about 15 Sv of water from the Pacific Ocean into the Indian Ocean; the heat flux ~~, also known as transport-weighted temperature ,~~ (i.e. the effective temperature of the total ~~ITF export is~~ throughflow) of the total ITF export was 17.6 °C during these three years (Sprintall et al., 2009).

The MC acts as a source of sensible heat for the atmosphere over land, and the geographical configuration of the MC redistributes ~~sea surface temperatures (SSTs)~~ heat in the western Pacific and the Indian Ocean; both the effect of sensible heat and the geography of the MC are crucial for the onset of the Walker Circulation (Dayem et al., 2007). The variation of the Walker Circulation leads to various kinds of periodic phenomena that modulate the climate of the MC, including the El Niño–Southern Oscillation (ENSO), the Indian Ocean Dipole (IOD) and the Pacific Decadal Oscillation (PDO). The MC forms the western boundary of the ENSO phenomenon. On the interannual scale, ENSO and IOD play important roles in modulating rainfall and the ITF transport by affecting zonal winds (Wang, 2019). During El Niño years, the easterly trade winds in the Pacific are weakened. As a result, rainfall is decreased and the ITF is weakened (Zhang et al., 2016; Yamanaka et al., 2018) with a peak-to-trough amplitude of about 5 Sv (Feng et al., 2018). During La Niña years, the situation is reversed. The positive phase of IOD normally occurs during the autumn of an El Niño developing year, which offsets the effects of El Niño on the ITF (Wang, 2019; Sprintall and Révelard, 2014). On decadal timescales, the PDO plays a dominant role in regulating the ITF (Wang, 2019; Li et al., 2018b). Similar to the effect of ENSO, in the warm phase of the PDO easterly trade winds become weaker, causing the ITF transport to ~~become weaker~~weaken, and vice versa (Wang, 2019). A modelling study from Tan et al. (2022) highlighted the importance of the geometry of the MC, and found that the shallow opening of the MC can trigger an active Pacific meridional overturning circulation and enhance upwelling strength along the equator from the Central to Eastern Pacific.

It is possible to obtain an "atlas" of the future warming world from climate model simulations (e.g. Iturbide et al. (2021); Gutiérrez et al. (2021)). However, there is no direct evidence for us to validate how well climate models simulate the future. The mid-Pliocene is an interval in the mid-Piacenzian between 3.264 and 3.025 million years (Ma) before ~~Present~~ present (BP). According to the Intergovernmental Panel on Climate Change (IPCC) Sixth Assessment Report (AR6) Working Group I (WGI) Technical Summary (Arias et al., 2021), the mid-Pliocene is *very likely* 2.5°C to 4.0°C warmer than the preindustrial, and the concentration of CO_2 during this period is *very likely* in the range from 360 ppmv to 420 ppmv, which is substantially higher than for the preindustrial period (280 ppmv). In terms of temperature ~~,~~ and geography, the Earth System of the mid-Pliocene is similar to projections for the end of the 21st century (Dowsett et al., 2016). Consequently, the mid-Pliocene is considered one of the most recent analogues to ~~the~~ future warm conditions on a broad scale perspective (Salzmann et al., 2009; Burke et al., 2018).

During the Pliocene Epoch, the Indonesian Gateway reorganized due to tectonic processes, and the ITF was restricted progressively (Karas et al., 2009; Auer et al., 2019). This process contributed to variations of climate throughout the mid-Pliocene. For example, during the mid to late Piacenzian (3.3 Ma –2.6 Ma BP), the reorganization of the ITF led to a strengthening of the South Asian Summer Monsoon and acted as a precursor to east African aridification (Cane and Molnar, 2001; Sarathchandraprasad et al., 2021). By using model results, we can explore the mid-Pliocene climate in this region. This effort is supported by geological records that provide a variety of evidence towards reconstructing the climate over the MC during the mid-Pliocene. For example, deep-sea deposit samples of the mid-Pliocene can be utilized to reconstruct ~~sea surface temperature (Wara et al., 2005; Zhang et al., 2014; Fedorov et al., 2015; O'Brien et al., 2014; McClymont et al., 2020)~~ SST (Wara et al., 2005; Zhang et al., 2014; O'Brien et al., 2014; Fedorov et al., 2015; McClymont et al., 2020). By comparing

results of simulations and geological records, we can validate climate models and gain confidence in projections of future climate if the models perform well for past warm climates.

The mid-Pliocene has been broadly studied; previous works by the Pliocene Research Interpretation and Synoptic Mapping (PRISM; e.g., Dowsett et al. (2013, 2016)) and the Pliocene Model Intercomparison Project (PlioMIP; e.g, Haywood et al. (2010, 2016a, 2020)) provide us with a large amount of paleoclimate reconstructions and simulations of environmental and climatic information. The second phase of PlioMIP (PlioMIP2), that this study relates to, is briefly described in section 2 of this paper. Large-scale climate features of the mid-Pliocene as derived from PlioMIP1 and PlioMIP2 are described in Haywood et al. (2013) and Haywood et al. (2020): On a global scale simulated annual averaged surface air temperature is elevated, with models suggesting an anomaly above the respective conditions of the preindustrial ~~range~~ that ranges between 1.84 and 3.6°C based on PlioMIP1 (coupled atmosphere–ocean climate models only) and between 1.7 and 5.2°C based on PlioMIP2; annual mean total precipitation rates are higher by 0.09-0.18 mm d^{-1} (PlioMIP1; coupled atmosphere–ocean climate models only) and 0.07-0.37 mm d^{-1} (PlioMIP2) in the mid-Pliocene. All the models from PlioMIP1 and PlioMIP2 simulated a clear polar amplification of the warming in the mid-Pliocene and show that the warming magnitude in the MC is less than the global average. Regarding precipitation changes in the region, the PlioMIP1 ensemble shows an increase over most parts of the MC, especially in the tropics (Fig. 3b in Haywood et al. (2013)). In contrast to PlioMIP1, PlioMIP2 shows spatially heterogeneous changes in precipitation over the MC (Fig. 5b in Haywood et al. (2020)). Moreover, there is an increase in precipitation minus evaporation over exposed continents across this region (Fig. 1 in Feng et al. (2022)). PlioMIP1 studies have shown that tropical overturning circulation slows down in the mid-Pliocene due to the changes of ~~sea surface temperature~~SST, and that the ascending branch of the Walker Circulation over the MC weakens (Corvec and Fletcher, 2017). In terms of climate variability, ENSO exists in the modelled mid-Pliocene, but the amplitude of ENSO is weaker than in the preindustrial. This inference is consistent from PlioMIP1 (Brierley, 2015) to PlioMIP2 (Oldeman et al., 2021). However, the mean zonal SST gradient does not decrease consistently across models in PlioMIP2 (Oldeman et al., 2021). Although the MC is important for regional and large-scale climate, there are relatively few studies of the mid-Pliocene focusing on the MC (e.g. Smith et al. (2020)), especially studies that use the state-of-the-art models.

In order to explore this issue further, in this paper we investigate the climate of the MC in the mid-Pliocene by employing PlioMIP2 simulations.

We study large-scale climate patterns (~~sea surface temperature~~SST, the net fresh water flux at the surface (precipitation minus evaporation; P-E), salinity at the sea surface (SOS) and wind stress) of the MC and investigate ocean circulation and strength of the ITF in the mid-Pliocene. Moreover, we assess the ability of the PlioMIP2 models to simulate the mid-Pliocene climate of the MC by cross-validating simulations and models with proxy reconstructions and reanalysis data. We investigate differences in predictions by individual models with a hierarchical clustering method.

The rest of the paper is organized as follows. Section 2 describes the PlioMIP2 models, experiment design and simulation data that are relevant to this study. Section 3 addresses the following 4 main ~~question~~questions:

- Q1. How do PlioMIP2 models perform in simulating the mid-Pliocene and preindustrial climate of the MC? (Section 3.1);

- Q2. ~~How were climate (sea surface temperature, net water flux into the surface, salinity at sea surface~~ What are characteristics of the climate (SST, P-E, SOS and wind stress) ~~shaped~~ of the MC in the mid-Pliocene ~~on the MC~~ in the PlioMIP2 simulations? (Section 3.2);

- Q3. Did the volume transport via the ITF intensify in the mid-Pliocene, and what were the characteristics of this throughflow? (Section 3.3);

- Q4. How can we best emphasize results from individual models that may otherwise disappear in the multimodel ensemble mean (MMM)~~, and avoid~~? There is duplication of biases shared by ~~model~~ models from the same family in the MMM although models' results from the same family can be substantially different. How can we avoid this bias duplication? (Section 3.4)

Finally, we discuss drivers for changes of the ITF and of the climate of the MC (Section 4.1); we summarize performance of individual models and of the MMM in simulating mid-Pliocene and pre-industrial climate (Section 4.2); and we address similarities and differences between results by individual models (Section 4.3).

2 PlioMIP2

In this section, we describe the PlioMIP2 models, experiments and the PlioMIP2 project. In section 2.1, we introduce the PlioMIP2 models and the development of models which participated in the PlioMIP phase 1 and phase 2. Then, the two core experiments of PlioMIP2 adopted in this study are described in terms of boundary conditions (section 2.2).

2.1 PlioMIP2 ~~models~~Models

PlioMIP (Haywood et al., 2011) is a project aimed at studying climate and environments of the late Pliocene. PlioMIP is part of the Palaeoclimate Modelling Intercomparison Project (PMIP). In consideration of the development of models and proxy data in the past years, this project has progressed to the ~~next~~ second phase (PlioMIP2) (Haywood et al., 2016b, 2020). In ~~the second~~ this ongoing phase, there are more models (17 models in comparison to 11 models that participated in PlioMIP phase 1). Most of the newly participating models are descendants of existing models. For example, CCSM4 participated in PlioMIP1. The models derived from it, CCSM4-Utr, CCSM4-UoT, CESM1.2 and CESM2, participated in the second phase; IPSLCM5A from the Institute Pierre-Simon Laplace (IPSL) participated in PlioMIP, and then joined PlioMIP2 with IPSLCM5A2 and IPSL-CM6A-LR; NorESM-L, which has been developed from CCSM4, participated in the first phase, and then participated in the second phase with NorESM1-F. The atmosphere-only model HadAM3 participated in PlioMIP1 as a component of the UK Hadley Centre atmosphere-ocean general circulation model HadCM3~~,~~; in PlioMIP2 it contributed via the "CMIP6-class" UK Met Office HadGEM3-GC31-LL (Williams et al., 2021), as well as via HadCM3 (Hunter et al., 2019). Refer to Table 1 ~~in Haywood et al. (2020)~~ which shows the components used in the ~~PlioMIP2~~ PlioMIP2 models. In terms of the atmospheric component and oceanic component, new model versions were developed in that the parameterization changed (~~CCSM4-Utr and~~ CCSM4-UoT (Peltier and Vettoretti, 2014) and CCSM4-Utr use a simplified version of ocean mixing scheme from CCSM4

with parameterization changes; NorESM1-F updated the parameterization from NorESM-L), model components were updated (CESM1.2 and CESM2 adopted the atmospheric components of CAM5 and CAM6), or the resolution has been enhanced (IPSL models; NorESM1-F applied the tripolar grid in the ocean component compared with NorESM-L). All these models have run

145   the core mid-Pliocene experiment (Eoi400) and provide the preindustrial experiment (E280) as a control simulation. Table 1 shows details of the 16 PlioMIP2 models and of HadGEM3. For more details on the 16 PlioMIP2 models, see Haywood et al. (2020).

Table 1: Details of the 16 PlioMIP2 models (Haywood et al., 2020) and of the HadGEM3 model used in this study.

Model ID	modelling centre responsible for simulation	Atmosphere component, resolution, and layers	Ocean component, resolution, and layers	equilibrium climate sensitivity (ECS)	PlioMIP2 Publication
CCSM4	National Centre for Atmospheric Research, US	CAM4 FV0.9°×1.25° L26 (Neale et al., 2010)	Parallel Ocean Program version 2 (POP2) G16 (∼ 1°) L60 (Danabasoglu et al., 2012)	3.2	(Feng et al., 2020a)
CCSM4-Utr	Utrecht University, the Netherlands	CAM4 FV2.5°× 1.9° L26	POP2 with parameterization changes G16 (∼ 1°) L60	3.2	(Baatsen et al., 2022)
CCSM4-UoT	University of Toronto, Canada	CAM4 FV0.9°×1.25° L26	POP2 with parameterization changes G16 (∼ 1°) L60	3.2	(Chandan and Peltier, 2017)
CESM1.2	National Centre for Atmospheric Research, US	CAM5 FV0.9°×1.25° L30 (Neale et al., 2010)	POP2 G16 (∼ 1°) L60	4.1	(Feng et al., 2020a)

CESM2	National Centre for Atmospheric Research, US	CAM6 FV0.9°×1.25° L32 (Danabasoglu et al., 2020)	POP2 with update on parameterization and schemes G16 (∼ 1°) L60 (Danabasoglu et al., 2020)	5.3	(Feng et al., 2020a)
COSMOS	Alfred ~~Wagner~~ Wegener Institute, Germany	ECHAM5 T31 (3.75°× 3.75°) L19 (Roeckner et al., 2003)	MPI-OM GR30 (3.0°× 1.8°) L40 (Marsland et al., 2003)	4.7	(Stepanek et al., 2020)
EC-Earth3.3	Stockholm University, Sweden	IFS cycle 36r4 T159 (∼1.125°× 1.125°) L62	NEMO3.3 ORAC1 (1°× 1°) L46 (Madec, 2012)	4.3	(Zhang et al., 2021a)
GISS-E2-1-G	Goddard Institute for Space Studies, US	2.0°× 2.5° L40 (Kelley et al., 2020)	GISS Ocean v1 1.0°× 1.25° L40 (Kelley et al., 2020)	3.3	n.a.
HadCM3	University of Leeds, UK	2.5°× 3.75° L19	1.25°× 1.25° L20	3.5	(Hunter et al., 2019)
HadGEM3	University of Bristol, UK	N96 (1.875°× 1.25°) L85	NEMO 3.6 1.0°× 1.0°L75	5.55	(Williams et al., 2021)
IPSLCM5A	Laboratoire des Sciences du Climat et de l'Environnement, France	LMDZ5 revision 2063 3.75°× 1.875° L39 (Hourdin et al., 2013)	NEMOv3.2 2.0°× 2.0°, 0.5°in the tropics L31 (Madec, 2012)	4.1	(Tan et al., 2020)
IPSLCM5A2	Laboratoire des Sciences du Climat et de l'Environnement, France	LMDZ5 revision 3342 3.75°× 1.875° L39 (Hourdin et al., 2013; Sepulchre et al., 2020)	NEMOv3.6 2.0°× 2.0°, 0.5°in the tropics L31 (Sepulchre et al., 2020)	3.6	(Tan et al., 2020)

IPSL-CM6A-LR	Laboratoire des Sciences du Climat et de l'Environnement, France	LMDZ6A-LR 2.5°× 1.26° L79 (Hourdin et al., 2020; Boucher et al., 2020)	NEMOv3.6 ~1°, latitudinal refined at 1/3°in the equatorial region L75 (Hourdin et al., 2020)	4.8	(Tan et al., 2020)
MIROC4m	University of Tokyo, Japan	T42 (~2.8°× 2.8°) L20	1.4°longitude, 0.56°-1.4°latitude L43	3.9	(Chan and Abe-Ouchi, 2020)
MRI-CGCM2.3	University of Tsukuba, Japan	T42 (~2.8°× 2.8°) L30	2.5°longitude, 2.0 - 0.5°latitude L26	2.8	(Kamae et al., 2016)
NorESM-L	NORCE Norwegian Research Centre, Bjerknes Centre for Climate Research, Norway	CAM4 Oslo version T31 (~3.75°× 3.75°) L26	Miami Isopycnic Coordinate Ocean Model (MICOM) G37 (~3.0°× 3.0°) L30	3.1	(Li et al., 2020)
NorESM1-F	NORCE Norwegian Research Centre, Bjerknes Centre for Climate Research, Norway	CAM4 Oslo version 1.9°× 2.5° L26	MICOM ~1.0°× 1.0°L53	2.3	(Li et al., 2020)
~~HadGEM3~~ ~~University of Bristol, UK N96 (1.875°× 1.25°) L85~~ ~~NEMO 3.6 1.0°× 1.0°L75~~ ~~5.55(Williams et al., 2021)~~					

Figure 1. PRISM4 Pliocene land-sea mask. The modern continental outline is indicated with black lines; blue and green shadings indicate ocean and land in the Eoi400 mid-Pliocene experiment. The red rectangle indicates the ~~gateway we defined in this work to calculate~~ location of the ~~intensity~~ Timor passage of the Indonesian Throughflow (ITF) that we refer to in section 3.3. The red arrow denotes the position and direction of the ITF illustratively. The Sunda and Sahul shelves are illustrated in this figure via white labels. The continental outline is constructed from Dowsett et al. (2016) and retrodicted with a set of procedures based on the paleogeographic maps of Markwick (2007).

2.2 PlioMIP2 Experimental Design

The global-scale and gridded paleo reconstruction data from PRISM provides data for mid-Pliocene paleo-geography and land ice, etc., to enable preparation of reliable boundary conditions and to carry out climate ~~models~~ simulations of the mid-Pliocene. For PlioMIP phase 1, experiment boundary conditions for the mid-Pliocene have been built based on PRISM3D (Dowsett et al., 2010). In PlioMIP2, new boundary conditions have been adopted, which are derived from the state-of-the-art reconstruction PRISM4 (Dowsett et al., 2016).

In this study we adopt the E280 simulation as a control experiment, which is forced with preindustrial conditions, and the Eoi400 simulation as a sensitivity experiment for mid-Pliocene conditions, which is forced with all mid-Pliocene boundary conditions; these are topography, ice sheets, soil, vegetation, lakes, land-sea mask and a concentration of 400 ppm of CO_2 in the atmosphere. Simulation naming follows the rules established by Haywood et al. (2016a). The numbers 280 and 400 indicate the CO_2 concentration; character o indicates changes to orography, bathymetry, land–sea mask, vegetation, lakes, and soils from the preindustrial model setup towards mid-Pliocene conditions in regions free of ice sheets today, character i indicates such changes ~~of~~ in regions of current ice sheets. Fig. 1 shows the land-sea masks used in the E280 and the Eoi400 experiments indicated by black lines and colours, respectively, and illustrates the location of the MC. From this map it is clear that in the mid-Pliocene, several modern ocean gateways were absent, such as the Bering Strait, the ~~connection between~~ water body connetcting Canada and Greenland (Canadian Arctic Archipelago), and some straits in the MC. Details of the experimental design are described by Haywood et al. (2016a). The initial conditions of ocean salinity are either derived from **?**, from an equilibrium state of the modern (control) simulation, or from the end of the PlioMIP1 experiment (Haywood et al., 2011). Note that HadGEM3 did not change the land sea mask in the Eoi400 experiment, and therefore for this model the various gateways are the same as in E280. Data from the experiments E280 and Eoi400 used in this study are from the PlioMIP2 dataset, ~~part of~~ which is available at https://esgf-node.llnl.gov/search/cmip6/ and https://geology.er.usgs.gov/egpsc/prism/7.2_pliomip2_data.html. In this study, the ~~majority of the~~ results are calculated across the final 100 model years of each simulation. Data has been regridded to a 1° × 1° grid in order to calculate ~~ensemble means~~ MMM and MCM; results for individual models are illustrated based on the original grids. The MC regional averaged value in this paper is calculated from region of 25°S-25°N and 80°E-170°E.

3 Results

In section 3.1, model results are compared to proxy reconstructions and reanalysis data to evaluate model performance for reproducing mid-Pliocene and modern climate. Furthermore, the multimodel mean method (MMM) is evaluated by comparing its results with those derived from individual models. Then in section 3.2, we illustrate the most relevant patterns of mean climate of the MC in mid-Pliocene relative to the preindustrial ~~level~~ in terms of ~~sea surface temperature~~ SST, precipitation minus evaporation, wind stress and salinity at the ocean surface. Subsequently, we analyse ~~the~~ oceanic circulation in the MC (section 3.3). Lastly, we introduce a new metric - the multi cluster mean (MCM), which takes the weight of models from the different clustering branches into consideration to better illustrate the results from multiple models (section 3.4). Finally, we present a comparison between the performance of the multi-cluster mean (MCM), the MMM and individual models.
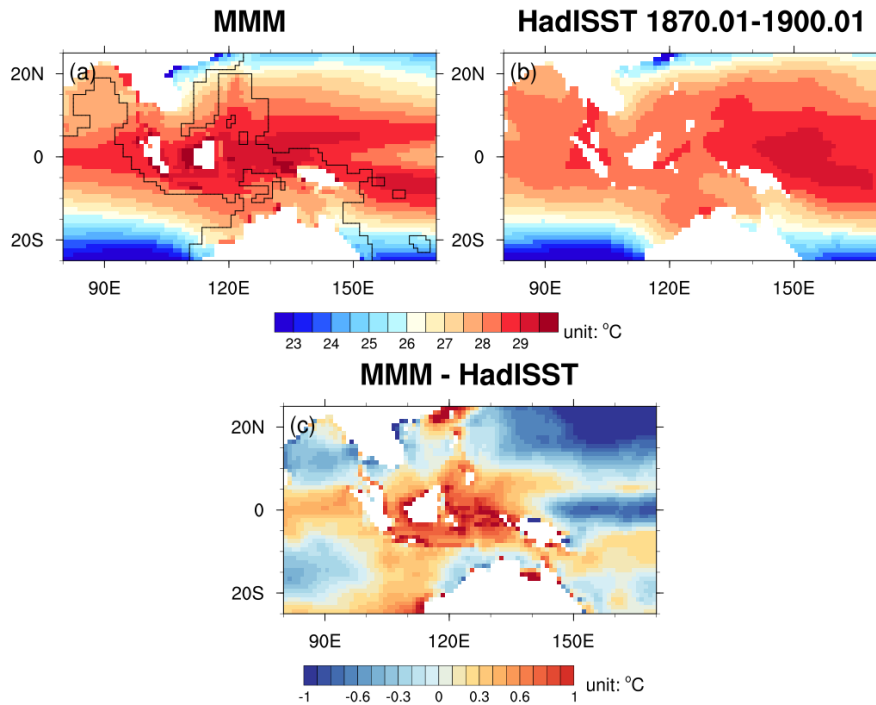
Figure 2. The annual mean sea surface temperature (SST) over the MC from: (a) PlioMIP2 multimodel ensemble mean (MMM) of the pre-industrial (E280), (b) HadISST1 reanalysed SSTs between January 1870 to January 1900 and (c) their difference. White shading indicates the grid boxes that are land for all the models. In (a), grid boxes outside the black lines are ocean grid boxes for all the models.

3.1   Model Skill at Simulating preindustrial and mid-Pliocene MC climate

In this section, we investigate how well a model performs in reproducing preindustrial climate (section 3.1.1) and mid-Pliocene climate (section 3.1.2). Our aim is to address the following questions: 1. Are the models that perform well in simulating preindustrial climate of the MC also good at simulating mid-Pliocene climate of the MC? 2. Does the multimodel ensemble have improved performance for the MC compared to individual models, as is often the case in weather and climate prediction (e.g.Tebaldi and Knutti (2007))?

3.1.1 Comparison with HadISST1

Observational data and reconstructed climatic information from proxy data can offer a way to evaluate simulation results. Here, we adopt the Hadley Centre sea ice and sea surface temperature (SST) reanalysis version 1 (HadISST1) (Rayner, 2003) from January 1870 to January 1900 to evaluate model performance in reproducing preindustrial climate. The HadISST1 dataset is available at https://www.metoffice.gov.uk/hadobs/hadisst/.

Fig. 2 shows the spatial distribution pattern of the preindustrial SSTs over the MC from the HadISST1 reanalysed SSTs and from the PlioMIP2 MMM. Despite that models reproduce the SST zonal gradient from the equator to higher latitudes, simulated SSTs are warmer surrounding the tropical islands and cooler in the North Western Pacific Ocean compared to the reanalysis data. By calculating the root mean square error (RMSE) between reanalysed SSTs and model SSTs over the MC, we quantify the model and observation discrepancy for the modern period, which is shown in Fig. S1 and Table S1 in the supplement. The mean discrepancy in the MC between the MMM SSTs and HadISST1 reanalysed SSTs is 0.51°C, which is lower (better) than 13 out of 17 models. By that metric, the MMM better reproduces preindustrial climate in this region than most of the individual PlioMIP2 models. The MMM metric also shows better agreement with observations than individual simulations in many other studies confer. Confer, for example, the study by R Williams et al. (2022) in the Deep-Time Model Intercomparison Project (DeepMIP), where the MMM is the best estimate of the actual precipitation in terms of spatial patterns relative to individual DeepMIP models.

In terms of individual models, CCSM4 shows the lowest discrepancy of any individual model (0.39°C); IPSLCM5A and HadCM3 show the highest discrepancies (1.29°C). In order to evaluate the simulated SSTs' spatial patterns, the discrepancy between the MMM SSTs and the HadISST1 reanalysed SSTs is also calculated after bias adjustment (i.e. removing the mean SST over the MC). The values are as shown in Table S1 Figure S1 in the supplement.
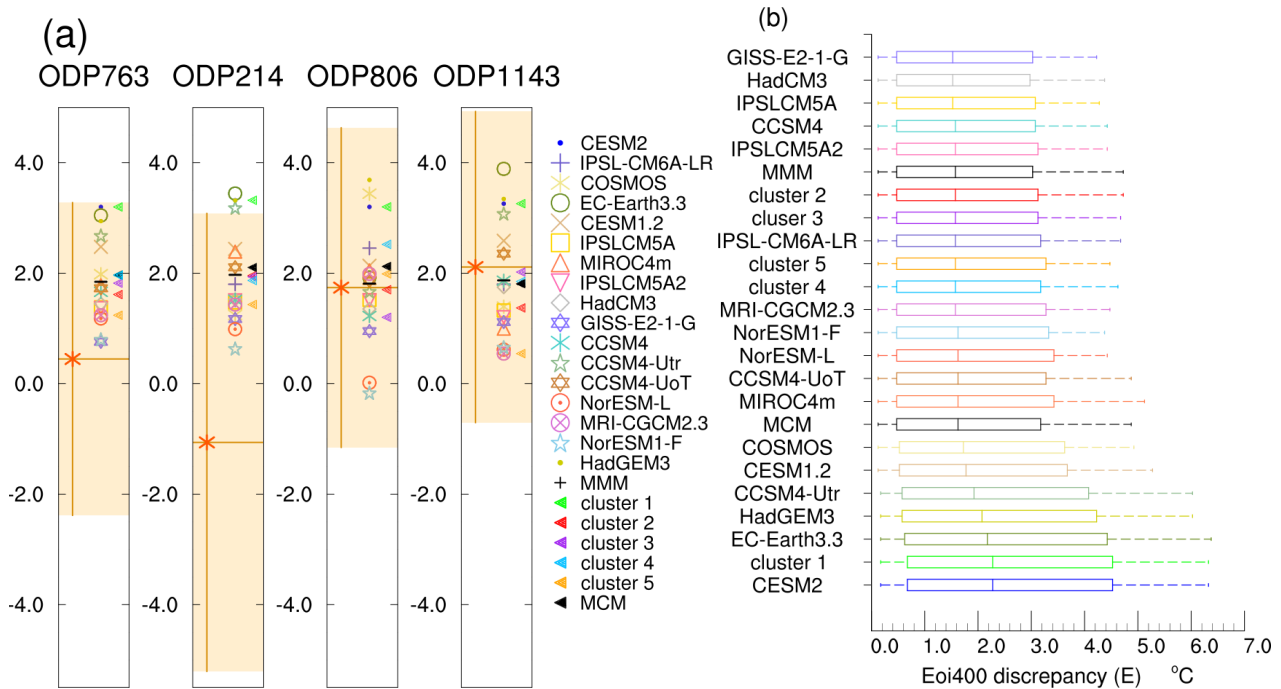
Figure 3. Discrepancy between modelled and reconstructed SST anomalies (SSTA) in the Pliocene. (a) Comparison between simulated and reconstructed SSTAs for 4 sites in the MC. The location of these 4 sites can be seen in Fig. 4a. The orange vertical bars and shading indicate the double standard errors ($\pm 2\sigma$) of the reconstructed SSTs. The orange horizontal bars and the asterisk indicate the reconstructed SSTAs of the site, individually. The short black horizontal bars among models' results indicate the MMM of the simulated SSTAs. ~~Triangles refer to the results by different clusters (colored) and to the MCM (black).~~ (b) Box-plot of model and proxy discrepancies over the MC for every model. Vertical lines inside the boxes are the median values (E) of the ~~possibility distribution~~ probability density function of the discrepancies derived via Monte-Carlo simulations, which is explained in section 3.1.2. Lower and upper box boundaries indicate the interval where the model and proxy discrepancies are *likely* to be (probability range from 66% to 100%). Lower and upper error ~~lines~~ bars indicate the interval where the model and proxy discrepancies are *most likely* to be (probability range from 90% to 100%). Models are ordered by their value of E. Also shown are the E values for the 5 clusters and the MCM.

3.1.2 Comparison with Pliocene proxies

For the mid-Pliocene, multi-proxy reconstructed SST anomalies (SSTA) data compiled by McClymont et al. (2020) are available for a narrow time slice centred on 3.205 Ma BP. This data (McClymont et al., 2020) is compared with the simulated mid-Pliocene SSTA in this study. Data and the full details for reconstructed SSTA are available at https://doi.pangaea.de/10.1594/PANGAEA.911847 and from McClymont et al. (2020). There are 4 sites with available data over the MC, as shown in Fig. 4a. The SSTA for ODP1143 is reconstructed from UK37 with the alkenone-derived (BAYSPLINE) calibration (Tierney and Tingley, 2018); the SSTA for ODP763, ODP214 and ODP806 are reconstructed from planktonic foraminifera *Trilobatus sacculifer* Mg/Ca with the Mg/Ca-derived (BAYMAG) calibration (Tierney et al., 2019a). Fig. 3a shows reconstructed and modelled SSTAs for every site individually. Model results for each site are provided as the average of the 9 grid boxes centred on the site in order to reduce regional bias. ~~For the site~~

There are large standard errors (σ) for the proxy reconstructed SSTAs, with $\pm 2\sigma$ shown with the orange shading in Fig. 3a. Models align well with the reconstructed SSTAs at site ODP806 in the WPWP and at site ODP1143 in the South China Sea. For the sites ODP763, ~~which is located close to the shore of the MC, and for the~~ ODP806, and ODP1143, all the models' results are within the uncertainties of reconstructions. For the site ODP214~~, which is located in the Indian Ocean, the models all simulate SSTAs that are warmer than the reconstructed data, especially for the BAYMAG-based SSTA estimate at site ODP214,~~ ~~the proxy data show that the Indian Ocean is cooler in the~~ a few (two) of models suggest comparably warm mid-Pliocene ~~than in the preindustrial, but all the models show a warmer SSTA~~ SSTA that are outside the uncertainty range of the reconstruction. We note that there is a persistent mismatch between Mg/Ca-derived (BAYMAG) and alkenone-derived (BAYSPLINE) SSTAs. McClymont et al. (2020) show that generally and with few exceptions, Mg/Ca-derived SSTAs are lower than their alkenone-based counterparts. In particular at lower latitudes there is a substantial mismatch~~, where~~. For example, at site ODP1143, which has both UK37 and Mg/Ca ~~even~~ data available, Mg/Ca suggests a negative ~~SSTAs~~ SSTA mid-Pliocene versus preindustrial, ~~that result from this proxy~~ is not supported by alkenones. ~~Furthermore, studies such as Zhang et al. (2014) and Smith et al. (2020) that reconstructed SSTAs from organic geochemical proxies also suggest that the SSTA in site ODP806 and region near the ITF outlet could potentially be warmer. In the models' results, simulated SSTAs over a broader region of the Indian Ocean surrounding the site ODP214 are all higher in the Eoi400 simulation than the E280 experiment. There are large standard errors (σ) for the proxy reconstructed SSTAs, with $\pm 2\sigma$ shown with the orange shading in Fig. 3a . Most of the models are within 2σ of the reconstructed SSTAs uncertainties. For the site ODP806 in the Pacific warm pool, the MMM SSTA (1.81°C) is very close to the reconstructed SSTAs (1.74°C); for the sites~~ For the Mg/Ca data at sites ODP763, ODP214 and ODP806~~, and ODP1143~~, ~~all~~ the ~~models' results are within the uncertainties of reconstructions. This implies that, in terms of SSTA, the models perform well at simulating the mid-Pliocene SSTAs over one site of the Western Pacific Warm Pool (WPWP) and the South China Sea, and also have skill in the Indian Ocean close to the coast of Australia. The exception is site~~ Mg/Ca-derived SSTAs are all cooler than the MMM SSTA. Especially at site ODP763 and at site ODP214, ~~where models have less skill in reproducing the SSTA of this site. A few of models suggest comparably warm~~ the reconstructed data show a cool bias compared to the simulated SSTAs from all the models. For site ODP214, in the Indian Ocean the proxy data even show the mid-Pliocene

SSTA that are outside the uncertainty range of the reconstruction. Yet, we note that relative cold SSTA is derived from SST that is cooler than in the preindustrial, but all the models show warmer SSTAs. The cold biases of the Mg/Ca-reconstruction at this site Ca-derived SSTAs can be attributed to some environmental factors, such as seasonality and the calcification depth of foraminifera (Hertzberg and Schmidt, 2013; Hönisch et al., 2013; Tierney et al., 2019b; McClymont et al., 2020), which can explain

245   larger biases in the tropics where the thermocline is relatively deeper than at higher latitudes. Moreover, the foraminifera *Trilobatus sacculifer* adopted in ODP214 and ODP763 broadly derives larger negative SST anomalies compared to another surface-dwelling warm water foraminifera *Globigerinoides ruber* in the study of McClymont et al. (2020), which aligns with results from some studies (Fairbanks et al., 1980; Ravelo and Fairbanks, 1992; Curry et al., 1983) that in the tropics *Trilobatus sacculifer* is often found in a slightly deeper habitat than *Globigerinoides ruber* (Tierney et al., 2019b). Furthermore, studies

250   such as Zhang et al. (2014) and Smith et al. (2020), that reconstructed SSTAs from organic geochemical proxies, also suggest that the SSTA in site ODP806 and region near the ITF outlet could potentially be warmer.

In order to quantify the discrepancies between proxy reconstructed and simulated SSTAs from individual models, we apply Monte-Carlo simulation similarly to (Kageyama et al., 2021). The results are shown in Fig. 3b, sorted in ascending order of model and proxy discrepancy median value E. Since there are uncertainties for proxy data, we generate an array containing

255   1000 random SSTAs using a uniform range distribution derived from the reconstructed SSTAs and $\pm 2\sigma$ for every site. Uncertainties of the simulated SSTAs are derived over the last 100 years of annual mean SSTAs. By subtracting the reconstructed SSTAs arrays from the 100 simulated SSTAs for every site separately , and combining the arrays for the 4 sites, we derive arrays of model and proxy discrepancy for individual models which contains contain 400,000 (1000×100×4) SSTAs. A box plot illustrating *likely* and *very likely* range of the probability density distribution function of the model and proxy absolute

260   discrepancy is shown for every model in Fig. 3b. The vertical lines inside the boxes are the medians of the probability density distribution function, which means that there is a probability of 50% that model and proxy discrepancy are less than this value. Here we use letter E to denote discrepancy. The box in Fig. 3b shows the range of the *likely* model and proxy discrepancy; the dash error bar shows the range of the *very likely* model and proxy discrepancy. The likelihood definition adopted here is that from the IPCC Guidance Note (Mastrandrea et al., 2010); *likely* means the probability of the outcome ranges from 66% to

265   100%; *very likely* means the probability of the outcome ranges from 90% to 100%. By using this method, we take uncertainties of proxy data and model simulation into account. From Fig. 3b we find that the E values between proxy and models range from 1.52°C to 2.28°C. As the majority of the model SSTAs show a warmer bias are warmer than the reconstructed SSTAs (Fig. 3a), the models showing relatively less regional warming also show a lower discrepancy value E with proxy SSTAs over the MC than the models that produce higher warming (Fig. S2). The PlioMIP2 models' MMM shows a discrepancy value E of

270   1.58°C, which is lower than that of most of the PlioMIP2 individual models.

Comparison of the model and data discrepancies between the E280 and Eoi400 simulations. Discrepancy values are as shown in Table S1. The unit is °C.

In order to explore whether those models, that perform well in simulating preindustrial SSTs over the MC, are also good at simulating the mid-Pliocene SSTAs over the MC, the discrepancies of models and observed SSTs on the one hand and recon-

275   structed SSTAs on the other hand for both experiments are shown in Fig. S3 for both experiments. In terms of simulating the cli-

mate of the MC, there is no clear correlation between model performance in preindustrial climate and in mid-Pliocene climate, implying that models, which reproduce preindustrial climate of the MC well, are not always good at simulating mid-Pliocene climate of the MC in accordance with the proxy reconstructions. However, ~~from~~ we note that the uncertainty of discrepancies between model and reconstructed SSTA in the MC is significant due to limited valid sites and high uncertainties of the proxy reconstruction. From Fig. S3, models ~~seems~~ seem to fall into two groups: models where the discrepancy in the Eoi400 experiment ~~appear decoupled from those~~ appears decoupled from that in the E280 experiment, and models where regional biases are linked between the E280 and Eoi400 simulations (including CESM2, EC-EARTH3.3, HadGEM3, NorESM1-F and CESM1.2). Models in the second group ~~are also appeared~~ also appear to be relatively warm in the Eoi400 simulation (Fig. 5). In terms of simulating the global SSTA, the comparison of the model and data discrepancies on global scale between the E280 and Eoi400 simulations is shown in Fig. S4, which shows a better correlation than the regional SST simulation.

3.2 Mean Climate Features

In this section, we describe the modelled mean climatic characteristics of the mid-Pliocene relative to the preindustrial over the MC in terms of SST, wind stress, ~~precipitation minus evaporation (~~P-E~~), and salinity at the ocean surface (SOS)~~, and SOS.
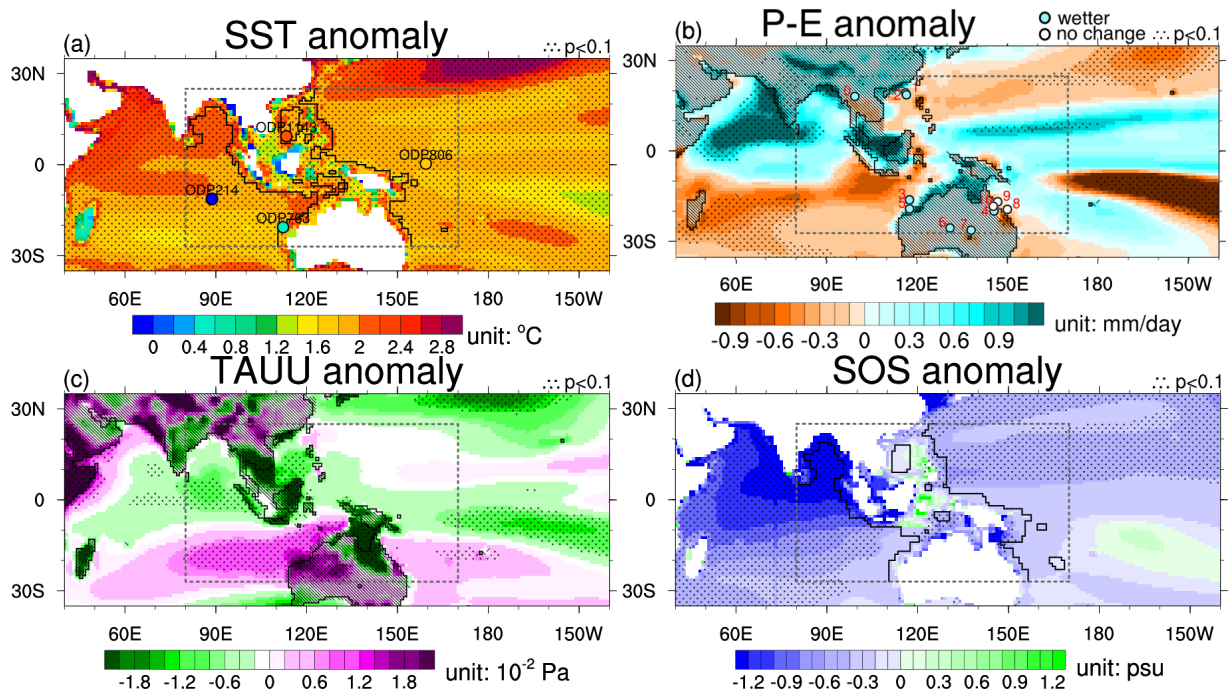
Figure 4. The MMM anomalies over the MC in the Eoi400 simulation relative to the E280 simulation for (a) sea surface temperature (SST), (b) precipitation minus evaporation (P-E), (c) zonal surface wind stress (TAUU) and (d) salinity at the ocean surface (SOS). In (a), circles mark the location of the SSTA proxies~~, their~~. Their colour represents the reconstructed SSTAs, the value of which is also shown in Fig. 3a, and the name of each site is indicated on the top of each circle. White shading and black lines in (a) and (d) are as in Fig. 2. In (b) and (c), ~~the hatchings~~ hatches indicate land grid boxes in the mid-Pliocene experiment; the black lines indicate the continental outlines of the preindustrial experiment. In (b), filled circles denote proxy data in terms of wetter, or no-change condition. Details of each numbered site are shown in Table S2 in the supplement. In (c), green shading indicates westward anomaly and purple shading indicates eastward anomaly. Stippled areas show significant multi-model differences according to a t-test at the 90% confidence level.

The MMM shows a regional averaged warm SSTA of 1.88°C over the MC, the spatial pattern of which is as shown in Fig. 4a: the ~~Western Pacific Warm Pool~~ WPWP and the southern sector of the Indian Ocean in the MC ~~warm less~~ the anomaly is less warm compared with other regions. SSTAs ~~warm most~~ are comparably warm over the North Indian Ocean in the MC region. Oceans surrounding the land masses of the MC also show ~~an apparent warming~~ apparently warm SSTAs, but this is not a robust signal because the models' land sea masks differ in the region of the MC. Models showing the greatest regional average ~~warmings~~ warm SSTAs in the MC also show the largest global averaged warmings (Fig. ??). The linear regression coefficient between regional (the MC) and global annual SSTAs is ~1.06, implying that the SSTAs over the MC change at a similar magnitude as global SSTAs. The SSTA spatial ~~pattern~~ patterns over the MC from individual models are shown in Fig. S5.

~~As shown in~~ Fig. 5 shows the correlation of equilibrium climate sensitivity (ECS) and MC SSTAs from models. Regarding the SSTAs, models consistently show warmer SSTs over the MC in the mid-Pliocene relative to the preindustrial; regional averaged SSTA range from 0.43°C produced by NorESM1-F to 3.33°C produced by HadGEM3. HadGEM3, EC-Earth3.3 and CESM2 all produce SSTAs exceeding 3°C, which ~~represents~~ representing the 3 largest warm anomalies in the region among the PlioMIP2 models; 3 of the lowest SSTAs, which are all less than 1°C, ~~come~~ are from NorESM1-F, NorESM-L, and MRI-CGCM2.3, which are also the models with the lowest equilibrium climate sensitivity (ECS) among PlioMIP2 models (Haywood et al., 2020) as shown in Fig. 5. ~~As~~ On long time scales, ECS is constrained by pattern effects i.e. radiative feedbacks change as SST patterns evolve (Ceppi and Gregory, 2017; Zhou et al., 2016; Armour, 2017; Gregory and Andrews, 2016; Dong et al., 2020). For CMIP5 models, the WPWP is a key region, a warming in this region dominates the difference of radiative feedback by enhancing Earth's albedo (Zhou et al., 2021; Dong et al., 2020). In the study of Haywood et al. (2020) which adopted CMIP6 and non-CMIP6 models, there is a relationship between models' ECS and their global temperature anomalies (Eoi400 minus E280) ~~in the study of Haywood et al. (2020), models' ECS correlates with~~. With the regard to warming of the WPWP in CMIP6 models, the MC contributes to the climate feedback differences, but there's a stronger sensitivity of extratropical clouds to surface warming that may result in differences(Dong et al., 2020). As such, the relationship of ECS and SSTAs on the MC ~~, but the linearity~~ is not exactly ~~linearly~~ linear. For example, GISS-E2-1-G shows an SSTA less than 1°C, but its ECS is relatively high. CCSM4-UoT and CCSM4-Utr have a modest ECS but show high global near-surface air temperature anomaly (Haywood et al., 2020) as well as a relatively high SSTA over the MC in mid-Pliocene ~~over the MC~~. The best fit line of the linear relationship between ECS and SSTAs on the MC is ECS=2.43°C+0.74xSSTA at the 95% confidence level with $R^2 = 0.56$.

The warmer MC SSTs not only influence the atmospheric circulation in the Pliocene but also bring higher evaporation due to higher water vapour holding capacity of ~~warmer~~ warm air (the Clausius-Clapeyron equation) and more atmospheric moisture, which contributes to the change of simulated precipitation. As an essential part of the hydrological cycle, freshwater budget over land and ocean ~~(precipitation minus evaporation) influences the oceanic~~ P-E) influences ocean salinity and shapes the climate of the MC. Fig. 4 illustrates the MMM anomalies of P-E, zonal wind stress (TAUU) and SOS over the MC in the mid-Pliocene relative to the preindustrial.

For the MMM P-E anomalies, if we take the MC as a whole, the ~~freshwater budget (~~P-E ~~)~~ is more positive in the mid-Pliocene over the MC relative to the preindustrial (Fig. 4b); 13 out of 17 models ~~,~~ and the MMM ~~,~~ consistently show an increase in P-E
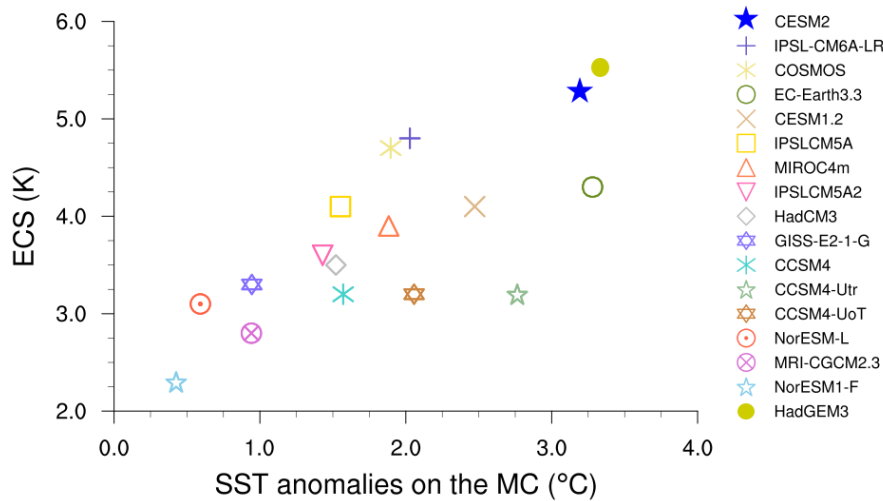
Figure 5. SST anomalies over the MC versus equilibrium climate sensitivity (ECS) from all the PlioMIP2 models.

(Fig. S6). As shown in Fig. 4b, it can be seen that unlike the SSTs, P-E does not change consistently over the MC but varies throughout the ~~MC~~region. P-E increases over the Western Pacific Ocean and the North Eastern Indian Ocean, but decreases evidently over the west oceanic sector of the MC gateway. From ~~the~~ hatching and black lines in Fig. 4b, the difference in the distribution of land and sea in the Eoi400 and the E280 simulations is evident. P-E increases over most lands of the MC, and also increases generally over grid cells which are ocean in the preindustrial but land in the mid-Pliocene, leading to a land bias of precipitation increase. The spatial patterns of P-E anomalies from individual models are quite different (Fig. S6). In the case of some models, the simulated P-E anomaly is nearly opposite to each other, such as for COSMOS and EC-Earth3.3. Even the same family of models can show different results (e.g., CCSM-Utr and CCSM-UoT).

A large amount of precipitation ~~releases~~ provides energy to the atmosphere by releasing a large amount of latent heat~~to the atmosphere~~, which fuels the atmospheric circulation. In order to explore the changes of atmospheric circulation over the MC, we analyse the ~~zonal surface wind stress (TAUU)~~ TAUU anomalies, as shown in Fig. 4c. Green shading indicates a westward anomaly. There are westward anomalies over the North Western Pacific Ocean and eastward anomalies over the ocean to the west of Australia. This means that the tropical trade wind has been enhanced on the side of the North ~~Western Pacific Warm Pool~~WPWP during the mid-Pliocene. This signal can be seen from half of available PlioMIP2 models (Fig. S7). There are extreme values over some regions which belonged to a land mass during the mid-Pliocene but have turned into ocean in modern times. The extreme values found there ~~might~~ may therefore result from the change of land-sea distribution that also impacts on the prevalence of surface roughness. The latter impacts atmospheric flow more over land than over ~~the~~ ocean.

As a result of the changes in the hydrological system, SOS changes ~~in the seas surrounding the~~ surround the MC. Fig. 4d illustrates the spatial distribution of SOS anomalies. We find a decrease of SOS in most of the ocean regions belonging to the MC. This pattern is especially pronounced in the northern part of the Indian Ocean, where one can find SOS to decrease by more than 1.2 PSU. For the Pacific Ocean sector and the southern Indian Ocean sector of the MC, SOS decreases by less than 1 PSU. Overall, we find that seawater becomes fresher at the surface around the MC in the mid-Pliocene in comparison to the preindustrial. This finding is consistent in 14 out of 16 PlioMIP2 models and in the MMM. Spatial patterns of SOS anomalies for individual models are shown for reference in Fig. S8.

3.3 Ocean Currents

Temperature and density differences are ~~drivers~~ factors that can make contribution to the change of the ITF, which is an important process for regulating the climate of the MC. As the seawater characteristics of Pacific Ocean and Indian Ocean are so different, oceanic flow through the MC does not only transport volume, but also creates a net-transport of salinity and heat between these two oceans. This process can directly influence both local and remote climate. Therefore, we quantify and investigate the changes of oceanic flow through the MC in the mid-Pliocene. In this section, we address the following questions: Is there more fresh and warm water injected into the Indian Ocean from the Pacific Ocean in the mid-Pliocene relative to the preindustrial? Where do the anomalies originate from? Do the anomalies result from the surface ocean, or rather from processes and characteristics that are shaped in deeper layers of the sea?
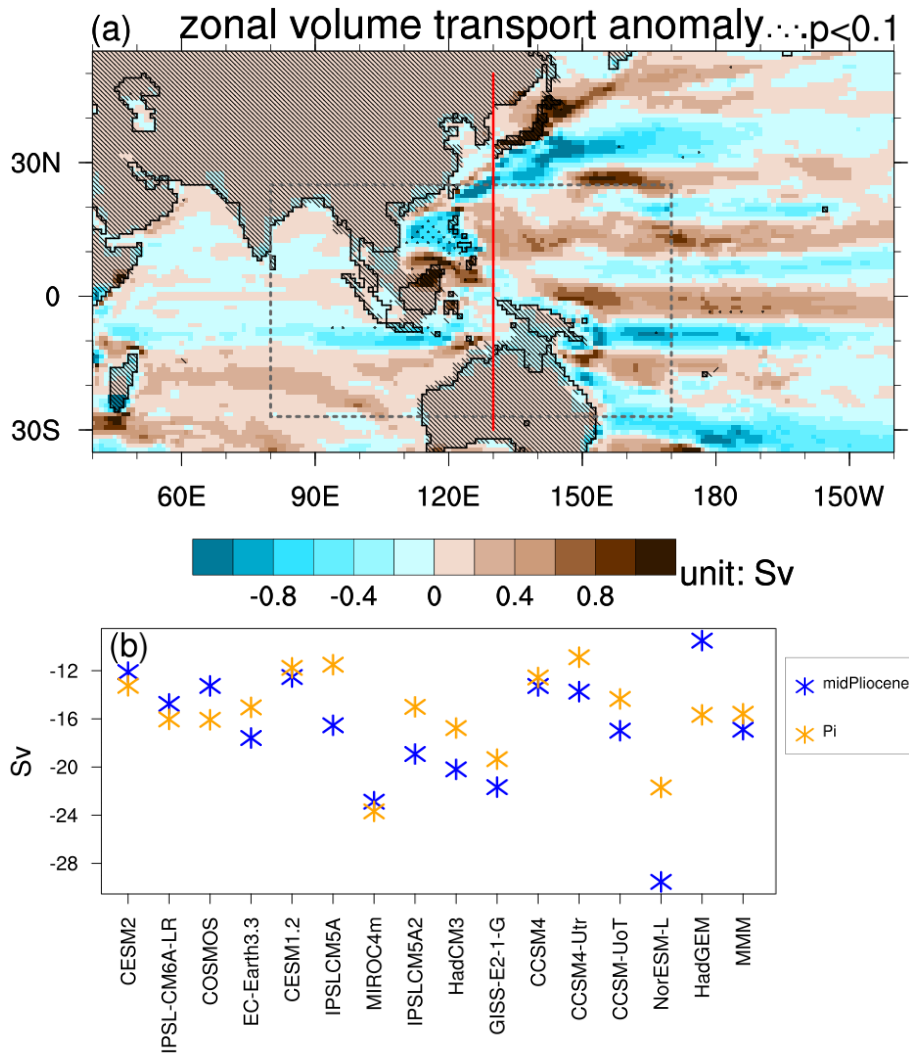
Figure 6. (a) The MMM zonal ~~sea water velocity (UO)~~ seawater volume transport anomaly in the Eoi400 experiment relative to the E280 experiment. Blue shading indicates westward anomaly and brown shading indicates eastward anomaly. The red ~~rectangle~~ line is the ~~gateway defined~~ transect to calculate the ocean volume transport intensity in (b). The ~~hatchings~~ hatches indicate land grid boxes in the mid-Pliocene experiment; the black lines indicate the continental outlines of the preindustrial experiment. (b) The integrated ocean volume transport intensity through the gateway. Negative values indicate westward transport. Stippled areas show significant multi-model differences according to a t-test at the 90% confidence level. The maps of zonal seawater volume transport for individual models are as shown in Fig. S12.

We study the oceanic flow with the available data. During the calculation of ocean currents, we find that there are some disagreements between results derived from regridded data and analyses performed on individual models' native ocean model grids. Therefore, to reduce errors and improve the accuracy, we use native grid data to calculate the oceanic flow intensity. ~~Fig. 1 shows the gateways (red rectangle), and differences in the land sea distribution between the E280 and the Eoi400 simulations.~~ In order to include all the seawater transport through this gate and keep consistence for all the models, we calculate the seawater volume transport through a broad transect as shown with the red line in Fig. 6a. In the modelled mid-Pliocene, some regions, which are islands in the preindustrial, are still a peninsula that is connected to the Asian mainland in some models (CESM2, EC-Earth3.3, CESM1.2, MIROC4m, HadCM3, GISS-E2-1-G, CCSM4, CCSM4-Utr and CCSM-UoT). In these models except for HadGEM3 which adopted the same land-sea mask of the MC in both experiments, the Malacca Strait, and some other small straits in the northern part of the MC, are closed as shown in Fig. 1. Except for this gateway, the strait between New Guinea and Australia is also closed. Therefore, the Sunda and Sahul shelves caused some straits of the modern MC, that are present in the E280 experiment, to be absent in the Eoi400 experiment. However, the volume transport through the Malacca Strait is very small compared with the volume transport through the main ITF passage. Therefore, we only take the main part of throughflow, that occurs through the gateway ~~showed~~ shown in Fig. 1, into account.

The spatial pattern of the vertical integrated zonal ~~velocity (UO)~~ seawater volume transport anomaly is shown in Fig. 6a. There is a westward ~~UO~~ transport anomaly along the northeastern coast of the New Guinea, which favours the ocean mass transport of the ITF. For the oceanic ~~velocity~~ transport through the gateway, the westward water transport has been strengthened over the north, but weakened over the south. Models and modern observation both show a strong flow through the gateway between MC and Australia. According to the observation between 2004 and 2006 (Sprintall et al., 2009), the ocean volume transport via the Indonesian Throughflow to the Indian Ocean is 15 Sv. By integrating the water volume transport through this gateway vertically, we derive the total seawater transport volume through the MC, which is shown in Fig. 6b. Based on the model results, the flow through the MC ranges from 10.9 Sv (CCSM4-Utr) to ~~19.6~~ 23.7 Sv (MIROC4m) westward in the preindustrial and from ~~8.8~~ 9.5 Sv (HadGEM3) to ~~24.3 Sv (MIROC4m~~ 29.5 Sv (NorESM-L) westward in the mid-Pliocene. The result of the E280 experiment from every model shows the same transport direction and a magnitude comparable to observations. Compared to the preindustrial, the strength of the flow shows ~~a clear~~ an increase in 10 out of 15 models, ranging from ~~12.2~~ 5.6% (~~IPSLCM5A) to 34.6~~ CCSM4) to 43.8% ~~(EC-Earth3.3). Exceptions are three very small changes simulated by CESM2 (2.5%), NorESM-L (0.5%) and IPSL-CM6A-LR (-1.3%), and two reductions that~~ IPSLCM5A). Five reductions are observed in the simulation by ~~COSMOS (-6.6%)~~ CESM2, IPSL-CM6A-LR, COSMOS, MIROC4m and HadGEM3~~(-38.5%)~~. As mentioned before, the gateway geometry in HadGEM3 is the same in both E280 and Eoi400 experiments, which may lead to a result different from those of the other models. Therefore, ~~all but three~~ 10/15 of the PlioMIP2 models show agreement on an increase in ocean volume transport through the MC in the mid-Pliocene in comparison to the preindustrial ~~. The volume transport of 10 out of 15 models is appreciably increased~~ (NorESM1-F and MRI-CGCM2.3 are absent). ~~Three~~ Five of 15 models ~~show very small changes in volume transport. There are only three models (~~(CESM2, IPSL-CM6A-LR, COSMOS, MIROC4m and HadGEM3) that disagrees with the rest of the ensemble on the sign of transport change~~, and only two of these predict that volume transport through the gateway changes in an appreciable manner.~~
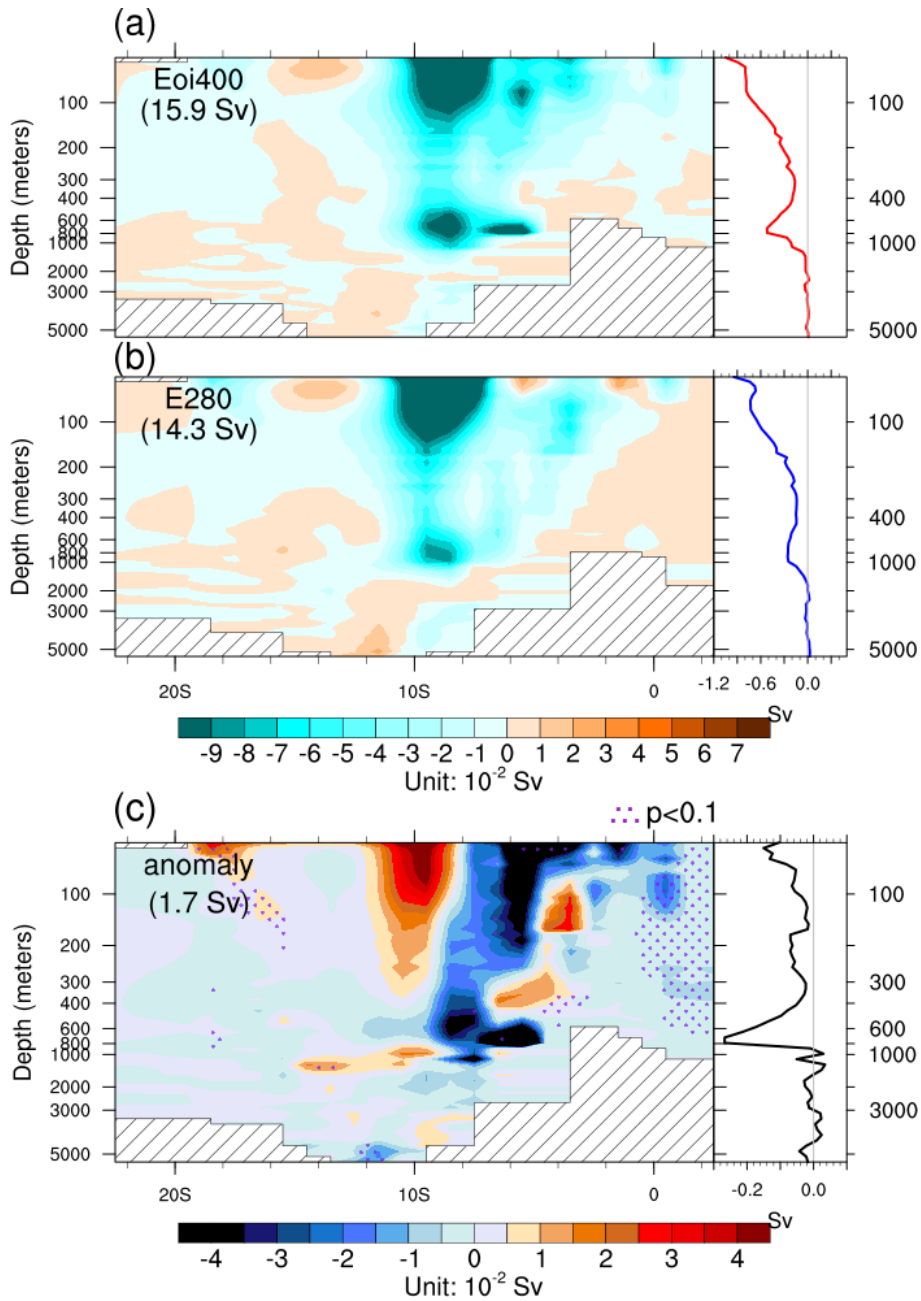
Figure 7. The MMM profiles of the ocean ~~current~~ volume transport through the MC in the mid-Pliocene (~~top panel~~a), in the preindustrial (~~middle panel~~b) and the anomalies of the mid-Pliocene relative to preindustrial (~~bottom panel~~c). The graphs attached on the right show the horizontally averaged ocean volume transport. Values in brackets indicate the total water volume transport through the gateway, positive value indicate westward transport. Warm shading indicates direction from west to east. Cold shading indicates direction from east to west. The ~~first~~ upper colour bar is for absolute values in ~~top panel~~ (a) and ~~middle panel~~(b). The colour bar on the bottom is for anomaly values in the ~~bottom panel~~(c). Stippled areas show significant multi-model differences according to a t-test at the 90% confidence level.

In order to explore which depth of the ocean determines the changes of throughflow, we investigate the vertical structure of water volume transport through ~~the gateway~~a broad passage of the ITF - Timor passage as shown by red line in Fig. 1, the MMM of which is shown in Fig. 7. In the MMM result, the strongest westward water transport is via the current located around

395    $10°S$. In general, the directions of water transport in the mid-Pliocene stay the same as for the preindustrial. This encompasses the westward transport through the main ITF passage as well as the relatively weak eastward transport through the south branch of the gateway simulated by some models (slightly yellow shading in Fig. 7). The strong westward flow counterbalances the weak eastward flow, and there is net-transport of fresh and warm water from the Pacific Ocean to the Indian Ocean. In both experiments, water mass is mainly transported in this gateway in the upper ocean above 1000 meters depth, which is consistent

400   from the results of the MMM and individual models (Fig. S9).

The profiles of the throughflow anomalies are shown in the bottom panel of Fig. 7. From the difference between Eoi400 experiment and E280 experiment~~in Fig. 7~~, it can be seen that the changes in meridional integrated ITF ~~changes~~ occur largely above 1000 meters depth, especially strongly at the surface and at a depth of around 800 meters, ~~without water transport direction reverse~~but without revolving the direction of water transport. In terms of the structure of the ITF anomaly, there is a

405   negative ~~anomaly~~ difference (stronger flow) in the northern part of the ITF and a positive ~~anomaly~~ change (weaker flow) ~~in the flow~~ between $12°S$ and $8°S$. This finding suggests that the ITF developed closer to the northern boundary of the gateway in the mid-Pliocene than it is located during the preindustrial at the layers above 1000 meters.

3.4 Clustering

So far we have studied the climatic features of the MC by using the multimodel ensemble method, which has often been em-

410   ployed when analysing results from multiple models. However, we have shown that, although models largely show agreement on warming and wetter climate over the MC in the mid-Pliocene, the spatial patterns of climate anomalies vary between models (e.g. Fig. S5). These differences might counterbalance each other to some extent, and therefore some important climate signals from individual models will be eliminated when using the MMM. Moreover, some of the employed models belong to a group of general circulation models that share model components or may be similar in other respects. Consequently, similar

415   signals from the same model family may be amplified in the ensemble of multimodel results. In order to investigate differences between models and to show the signals which might disappear in the MMM, we use clustering analyses in this section. Thereafter, we introduce a new metric, the multi cluster mean (MCM).

In the beginning of this section, we demonstrate the method of classifying models into groups based on the spatial features of SSTAs and precipitation anomalies over the MC from individual models by applying pattern correlation and the hierarchical

420   clustering method, which are derived for example from Sierra et al. (2017) and Knutti et al. (2013a). After averaging the results from multiple clusters, we obtain the MCM results. Then we illustrate the spatial anomaly pattern of every group and of the MCM, and compare them with the MMM. After that, we investigate the performance of cluster groups and of the MCM at the example of the mid-Pliocene and the preindustrial simulation, and investigate if these show less discrepancy with observation/reconstruction than the MMM.
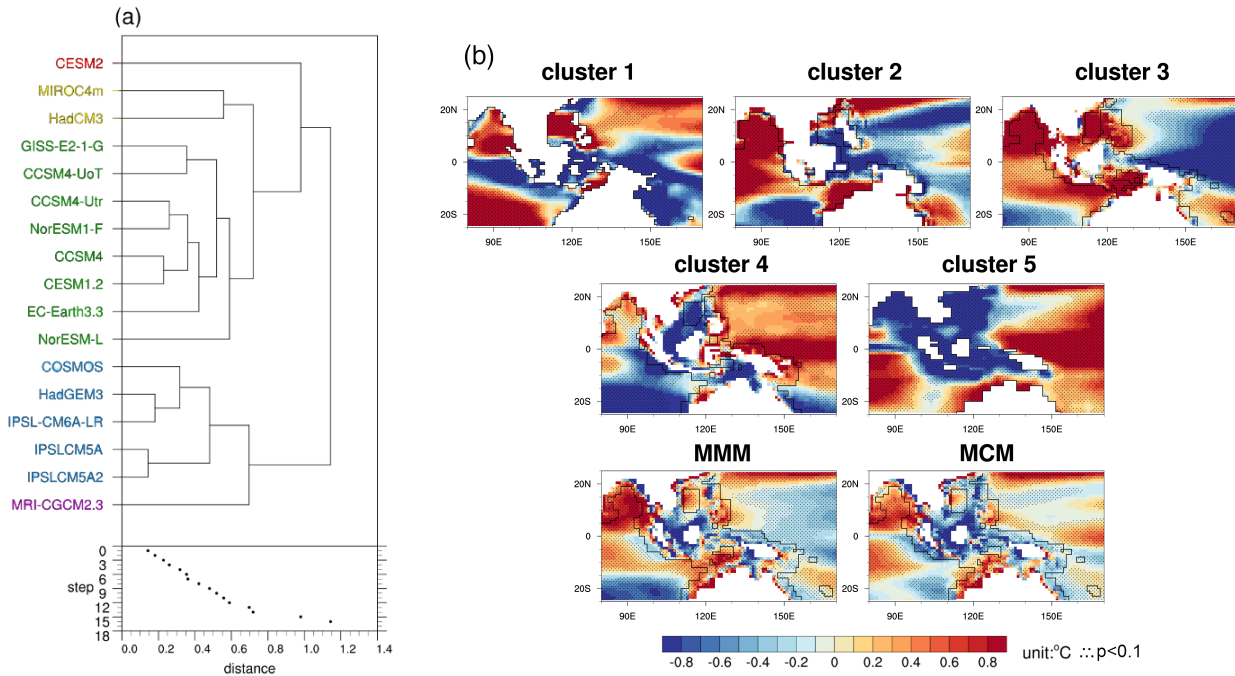
Figure 8. (a) Dendrogram of the SSTA clustering analysis based on the regional SSTAs over the MC from 17 PlioMIP2 models. Below the dendrogram the clustering step is shown as a function of distance between groups. (b) The SSTA patterns of the composite for different clusters, multi-model mean (MMM) and the multi cluster mean (MCM) after removing the regional mean SSTA. Cluster 1: CESM2; Cluster 2: MIROC4m and HadCM3; Cluster 3: GISS-E2-1-G, CCSM4-UoT, CCSM4-Utr, NorESM1-F, CCSM4, CESM1.2, EC-Earth3.3 and NorESM-L; Cluster 4: COSMOS, HadGEM3, IPSL-CM6A-LR, IPSLCM5A and IPSLCM5A2; Cluster 5:MRI-CGCM2.3. White shading indicates the grid boxes that are land for all the models of the cluster. The grid boxes outside the black lines are ocean grid boxes for all the models of the cluster. Stippled areas show significant differences according to a t-test at the 90% confidence level.

425   Fig. 8a and Fig. 9a illustrate the procedures of clustering. The first step is to find the two models with the smallest distance and join them into one group. On each subsequent step, the two closest groups or models are merged into a larger group. The distance between two models is the pattern correlation between the multiannual mean SSTAs or precipitation anomalies of these two models. The x-axes of the Fig. 8a and the Fig. 9a indicate the distance of every two joined groups at every step. The pattern correlation measures the similarity of the spatial patterns between two models (Taylor, 2001), which is the Pearson

430   Correlation Coefficient of the same variable of two different maps from two models. Here, for SSTAs we only use grid boxes which are ocean in all the models. ~~Here we~~ We choose average-linkage method (Wilks, 2011) to merge groups, which means the ~~distances between every~~ distance between two group is the averaged distance between individual members of the ~~two~~ groups.

In the bottom panel of Fig. 8a, ~~there is~~ we find a large jump after clustering steps 12, suggesting an appropriate stopping point with 5 groups, the group members of which are shown in Fig. 8a. CESM2 shows an SSTA spatial pattern that ~~different from~~ is different from that of the other PlioMIP2 models~~, that~~. Consequently it forms cluster 1 on its own. The same is true for MRI-CGCM2.3, but this model could be merged into another cluster if we moved one step forward. Cluster 2 contains MIROC4m and HadCM3. Cluster 3 contains the largest number of models, with 8 members, including almost all the CCSM series model (except for CESM2), NorESM series ~~model~~models, GISS-E2-1-G and EC-Earth3.3. IPSLCM5A2 is an updated version of IPSLCM5A in terms of updated components and technical characteristics (Sepulchre et al., 2020). This is clearly shown in the clustering results, with IPSLCM5A and IPSLCM5A2 being the two closest models. All the 3 IPSLCM models have been classified into cluster 4 together with COSMOS and HadGEM3. Fig. 8b illustrates the ensemble SSTAs pattern of every cluster after removing the regional mean SSTA. Cluster 4 and cluster 5 show a relatively warmer pattern on the WPWP, which is opposite to results present in cluster 3. For the Indian Ocean, cluster 4 shows a relative weak warm pattern, which means the Indian Ocean warms less than the region, especially the WPWP. Spatial distributions of SSTA in the Indian Ocean are similar for clusters 3 and 2, warmer in the north but less warm in the south, which is opposite to results from cluster 5. Since models are equally weighted in the ensemble, and cluster 3 contains the largest number of PlioMIP2 models, it dominates the MMM SSTA pattern (Fig. 8b). The MCM is the mean of these 5 clusters - in other words, it is the multimodel mean with weights. The MCM can avoid signals being overweighted from the same model family~~and demonstrate signals which disappear in the MMM~~; it conserves details of different types of climate realization, that may come from similar or very different models. For example, the centre of the WPWP shows a warmer anomaly, a result consistent for all clusters except for cluster 3. Comparison between warming of the WPWP and the eastern Indian Ocean on different clusters indicates 3 possible SSTA patterns: the eastern Indian Ocean warms more than the WPWP (cluster 2, cluster 3 and the MMM); the eastern Indian Ocean warms less than the WPWP (cluster 4); there is no apparent difference in warming between these two regions (cluster 1, cluster 5 and the MCM).
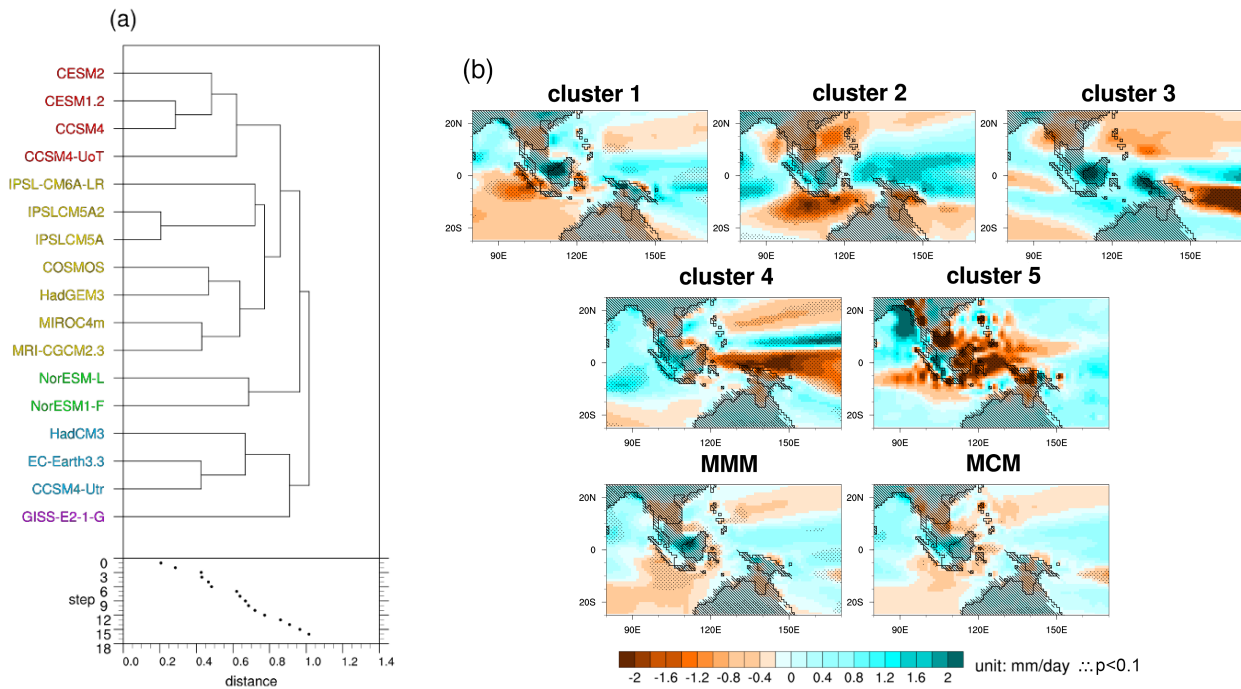
Figure 9. The same as Fig. 8 but for precipitation. Cluster 1: CESM2, CESM1.2, CCSM4 and CCSM4-UoT ; Cluster 2: IPSL-CM6A-LR, IPSLCM5A2, IPSLCM5A, COSMOS, HadGEM3, MIROC4m and MRI-CGCM2.3 ; Cluster 3: NorESM-L and NorESM1-F ; Cluster 4: HadCM3, EC-Earth3.3 and CCSM4-Utr ; Cluster 5: GISS-E2-1-G. The hatchings and the black lines are the same as Fig. 4. Stippled areas show significant differences according to a t-test at the 90% confidence level.
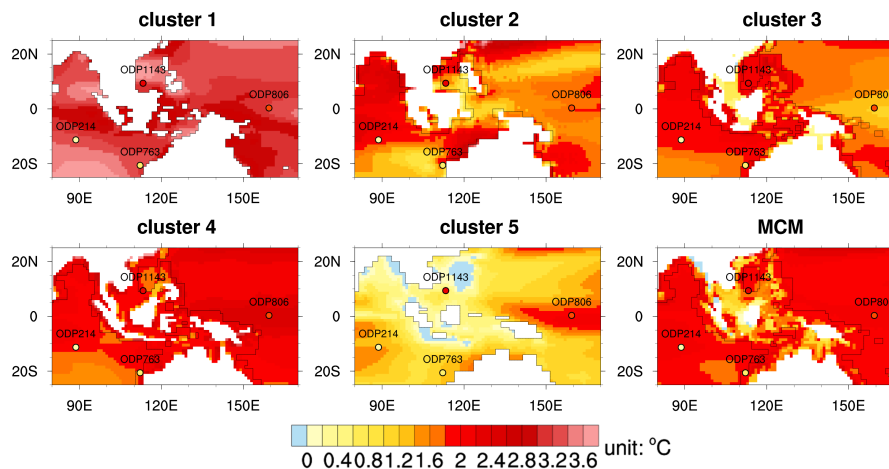
Figure 10. Comparison of reconstucted and modelled SSTAs over the MC in the mid-Pliocene (Eoi400) relative to the preindustrial (E280) from the SSTA-based clusters and the multi cluster mean (MCM). Cluster 1: CESM2; Cluster 2: MIROC4m and HadCM3; Cluster 3: GISS-E2-1-G, CCSM4-UoT, CCSM4-Utr, NorESM1-F, CCSM4, CESM1.2, EC-Earth3.3 and NorESM-L; Cluster 4: COSMOS, HadGEM3, IPSL-CM6A-LR, IPSLCM5A and IPSLCM5A2; Cluster 5:MRI-CGCM2.3. Units: °C. The MMM SSTAs ~~is~~ shown in Fig. 4a. Note that in this figure, regional averaged SSTA has not been removed as in Fig. 8b. White shading and black lines are the same as in Fig. 8b

In addition to the cluster based on SSTAs, we also sort models based on the precipitation anomaly spatial patterns, as shown in Fig. 9. Similar to SSTA analyses, we find a jump after step 12. Therefore, we classify the models into 5 groups (Fig. 9a). Four of the CCSM series models, CESM2, CESM1.2, CCSM4 and CCSM-UoT, form cluster 1. The IPSLCM-type models are members of the cluster 2 together with COSMOS, HadGEM3, MIROC4m and MRI-CGCM2.3. This cluster is the biggest one with 7 models. Similar to clustering based on SSTA, IPSLCM5A and IPSLCM5A2 are still the two most similar models; they are also the closest group for IPSL-CM6A-LR. NorESM-L and NorESM1-F form cluster 3. The remaining model in the CCSM series, CCSM4-Utr, joins EC-Earth3.3 and HadCM3 as cluster 4. For precipitation, cluster 5 (only GISS-E2-1-G) itself show a decrease in precipitation over the centre of the MC. For the WPWP, cluster 1 and cluster 2 show relatively wetter anomalies; cluster 3 and cluster 4 show basically drier anomalies with spatial heterogeneity. Cluster 5, which only contains GISS-E2-1-G, shows a ~~relative~~ relatively drier climate in the northwest but wetter ~~condition~~ conditions in the rest of the WPWP. All clusters except cluster 5 show a relative dry anomaly over the north of the WPWP. Similar to SSTA-based clustering, the cluster with the largest number of models dominates the spatial pattern of the MMM and leads some signals of other clusters to disappear. Overall, compared with the eastern Indian Ocean, the WPWP is relatively wetter (cluster 1, cluster 2, the MMM and the MCM), drier (cluster 3 and cluster 4), or receives similar ~~amount~~ amounts of precipitation (cluster 5). ~~Compared~~ If we compare Fig. 8b with Fig. 9b, the pattern of the MCM is more similar to the pattern of the MMM in precipitation than in the SSTA.

Fig. 10 compares the 5 clusters with the reconstructed SSTA data. In order to quantify model clusters' performance in simulating the mid-Pliocene SSTAs, the SSTA-based clusters are validated in the same way as individual models and as the MMM, as shown in Fig. 3 and Fig. S3. The performance of the MCM is similar to the MMM for every site. However, in contrast to the MMM, the MCM can take the model weight into account to avoid duplication of model signals from the same family, and also retain the climate signals we might lose in the multimodel ensemble. An example is the warm anomaly signal in the centre of the Western Pacific Ocean.

4 Discussion

4.1 Physical Mechanisms

The MC is a region of the atmospheric-oceanic coupling and exchange, slight changes here will affect climate afar (Gordon, 2005b; Yoneyama and Zhang, 2020). Due to the different land distribution, topography, and CO_2 concentration in the mid-Pliocene compared to today, we find that characteristics of mid-Pliocene climate of the MC, such as warmer SSTs, higher freshwater budget, lower SOS, strengthened surface zonal wind in WPWP and increased volume transport through the MC differ in comparison to the preindustrial.

~~In terms of atmospheric circulation, PlioMIP1 suggests weakening of the Walker Circulation in the~~ In the mid-Pliocene ~~(Corvec and Fletch~~ ~~; in~~ , wind and large scale atmospheric circulations change in responses to an overall warmer climate. According to the PlioMIP2 ~~this circulation change proved to be highly model dependent (Han et al., 2021). However, a robust feature across PlioMIP2 models is the westward shift of the Pacific Walker Circulation (Han et al., 2021). Moreover~~ simulations, the Northern Hemisphere warms more than the Southern Hemisphere ~~in the mid-Pliocene~~ (Haywood et al., 2020). As a result of the variation of interhemispheric meridional heat fluxes and energetic constraints for the Intertropical Convergence Zone (ITCZ) position, the Southern Hemisphere Subtropical High pressure system is intensified, and the western Pacific easterly trade is enhanced correspondingly (Pontes et al., 2021), which is consistent with the strengthened zonal wind stress we find in Fig. 4c.

~~Warmer SST in the~~ In terms of atmospheric circulation, the Walker Circulation consistently shows a westward shift within PlioMIP2 models, but the change in the strength proved to be highly model dependent (Han et al., 2021). In contrast, PlioMIP1 models suggested a weakened Walker Circulation in the mid-Pliocene ~~results in higher atmospheric moisture content (Allen and Ingram, 20~~ ~~. The warm West Pacific provides substantial water vapour that contributes to increased precipitation over the MC as part of the "wet-gets-wetter, dry-gets-drier" response, the spatial precipitation anomaly spatial pattern forms as shown in Fig. 4b (Feng et al., 2022).~~ in relative to the pre-industrial (Corvec and Fletcher, 2017).

~~In the mid-Pliocene,~~ On multi-decadal timescales, the Pacific trade wind system plays a role on the circulation strength and patterns within the MC and Indian Oceans (Sprintall et al., 2014; Vecchi and Soden, 2007). This has been observed in the 1970s when the weakening of the trade winds resulted in the western Pacific shoaling thermocline anomalies (Vecchi et al., 2006; Wainwright et al , and this anomaly can be transmitted to the Indian Ocean by the ITF (Alory et al., 2007). Results from coupled models also reveal that the strength of the ITF reduced correspondingly with the weakened Pacific trade winds (Sprintall et al., 2014). On the projected anthropogenic warming world, most models suggest a reduction in the equatorial trade winds and a decreased ITF

transport (Sen Gupta et al., 2012). In our study, most models show an increased ITF transport and also suggest an intensified

505 western equatorial Pacific zonal wind stress (Fig. S10). The wind can influence water properties, thermocline and sea level through wave processes and therefore impact the formation of the WPWP (Wijffels and Meyers, 2004; Drushka et al., 2010; Pujiana et al., 2. Changes in the WPWP have direct effect on the ITF, as the ITF is driven by the sea-level gradient between the western Pacific (high sea surface height) and the eastern Indian Ocean (low sea surface height) (Wyrtki, 1987; Sun and Thompson, 2020; Gordon, 2005a). On decadal timescales, the Pacific Ocean sea surface height (SSH) variability controls more than 85% of ITF variation

510 according to ocean reanalysis data (1959–2015) (Shilimkar et al., 2022). Here, we also correlated the annual ITF volume transport with annual SSH by using data from 4 available models as shown in Fig. S11. We find that generally the western Pacific SSH is positive correlated with the ITF. Furthermore, the SSH gradient between the western Pacific and the eastern Indian Ocean correlates well with the ITF in both E280 and Eoi400 experiments of GISS-E2-1-G and Eoi400 experiments of CESM2 and IPSL-CM6A-LR, but it has insignificant correlation with the ITF in Eoi400 experiment of EC-Earth3.3 as shown

515 by values on the top right of Fig. S11. Moreover, the ~~subaerial Sunda and Sahul shelves inhibit volume transport between western Pacific Ocean and Indian Ocean to some extent. However, the strengthened westward zonal wind stress over the Western Tropical Pacific Ocean changes sea level and thermocline via Kelvin and Rossby waves (Wang, 2019; Wijffels and Meyers, 2004) and is therefore favourable for water transport through the MC (Wainwright et al., 2008). This is consistent with the intensified ITF found in our study (Fig. 6b). In addition, over the northwest coast of Australia, the modelled wind stress shows an eastward~~

520 ~~anomaly (Fig. 4c). From the MMM zonal ocean velocity anomaly, there is also an eastward anomaly on the southern part of the ITF (Fig. 6a)~~ regions where SSH correlates with the ITF, differ between experiments and models. For CESM2, for example, experiments Eoi400 and E280 show different spatial patterns of the correlation coefficient map. However, models that show increased ITF in the Eoi400 do not always show an increase in SSH gradient and vice versa, implying at least for these four models, changes in the SSH gradient are not robust drivers for changes in the ITF between the mid-Pliocene and the

525 preindustrial.

The ITF can transfer the impact of ENSO to the Indian Ocean and further afar. As shown in a study of ENSO from PlioMIP2, models GISS-E2-1-G, COSMOS, IPSLCM6A and CESM2 show an 'El Niño-like' mean state, while CCSM4-Utr, ~~maybe as a result from the~~ EC-Earth3.3 and CCSM4 show a 'La Niña-like' mean state in the mid-Pliocene compared to the modern Pacific Ocean (Oldeman et al., 2021). All the models that show a clear 'La Niña-like' mean state also show stronger Pacific

530 Walker Circulation (Figure 10a from Han et al. (2021)) and corresponding intensified ITF; IPSLCM6A, CESM2, COSMOS and HadGEM3 show 'El Niño-like' mean states at weakened ITF. Although GISS-E2-1-G shows an 'El Niño-like' mean state and unspecific zonal wind stress ~~(Fig.~~ changes over the western tropical Pacific Ocean, it produces a stronger ITF. The rest of the models (IPSLCM5A, CESM1.2, HadCM3, NorESM-L) with intensified ITF, and MIROC4m with slightly weakened ITF, show a slight 'La Niña-like' mean state; IPSLCM5A2 and CCSM-UoT with intensified ITF show a slight 'El Niño-like' mean

535 state (Oldeman et al., 2021) (Figure 4c). ~~Based on observations, the variations of trade wind in the Pacific Ocean can explain changes of the ITF for the past decades (Feng et al., 2018). However, under global warming, the weakening of the ITF is more associated with~~

The ITF as a component of the global ocean circulation system also interacts with other circulations. In PlioMIP2, most models simulate a stronger Atlantic Meridional Overturning Circulation (AMOC) in the mid-Pliocene than the preindustrial (Zhang et al., 2021b; Weiffenbach et al., 2023). On the centennial scale, the ITF decreases if AMOC slows down as a northward surface flux anomaly converges ocean mass and increases SSH of the Indian Ocean (Sun and Thompson, 2020). Yet, as discussed for SSH above, debates of the connection of changes in AMOC and ITF remains to be studied. Nevertheless, in the study of simulated future CO_2 induced warming world, changes of the overturning circulation in the Pacific basin ~~: the zonal volume convergence via southern Australia decreases. Then upwelling increases to compensate for upper layer water, but transport into the deep~~ explain the change of the ITF (Sen Gupta et al., 2016). The northward flow of deep waters entering the Pacific basin at ~~the latitude~~ 40°S is weakened, and associated net basin-wide upwelling to the north of the southern tip of Australia ~~will decrease~~decreases, ultimately reducing the ITF (Fig. ~~10~~ S10 in Sen Gupta et al. (2016)). ~~The mechanisms of the changes of ITF in the~~ In mid-Pliocene~~remains a question to be studied in future work.~~, the Bering Strait is closed, water cannot be transport through this gateway and thus can contribute to the increased ITF volume transport. Except for the Bering Strait, the volume transport through south Pacific basin also be checked (Fig. S15). We find that models show decreased ITF volume transport are all show decreased volume transport through south Pacific basin in the mid-Pliocene relative to the preindustrial, either decreases on the shallow or the deep layer. For models showing increased ITF volume transport, the closed Bering Strait plays a role as the water leave the Pacific Ocean decreased, except for the HadCM3, which shows insignificant water transport via Bering Strait in the preindustrial. All models with increased ITF volume transport but GISS-E2-1-G show positive anomaly of the volume transport through south Pacific basin above 2000 meters in the mid-Pliocene relative to the preindustrial, and it can contribute to the increased ITF volume transport.

The ITF can not only be impacted by but also impact on the state of the surrounding oceans (Auer et al., 2019; Brierley and Fedorov, 2016). By comparing simulations with the MC gateways closed and opened, the removal of the ITF leads the SST in the tropical Pacific to increase and the SST of the southern Indian Ocean to decrease (Lee et al., 2002). Moreover, simulations where the ITF is blocked also show an eastward shift in atmospheric deep convection and precipitation in response to the warmer Pacific SST (Sprintall et al., 2014). In the mid-Pliocene, the substantially increased western Pacific SST results in higher atmospheric moisture content (Allen and Ingram, 2002), which provides substantial water vapour that contributes to increased precipitation over the MC as part of the "wet-gets-wetter, dry-gets-drier" response. As a consequence of multiple factors, the spatial precipitation anomaly pattern forms as shown in Fig. 4b (Feng et al., 2022).

Precipitation minus evaporation is the largest freshwater component entering the ocean (Byrne et al., 2016). Increased fresh water flux provides a way to explain the general decrease of the SOS over the MC, especially the decreased SOS in the Northern Indian Ocean. The changes of topography also play an important role. The closure of the gateway between New Guinea and Australia can change the water source from the saline south Pacific to the less saline north Pacific (Cane and Molnar, 2001), which can cause the Northern Indian Ocean SOS to decrease significantly. Furthermore, ~~the~~ higher precipitation and wetter climate over the Sunda shelves, India, south slope of the Tibetan Plateau and the surrounding regions (as shown in Fig. 5b of Haywood et al. (2020) and Fig. 1b of Feng et al. (2022)) may increase the local run-off, which can also inject more fresh water into the ocean and then dilute salinity.

Large scale flow patterns on the other hand seem to be simulated unambiguously across the PlioMIP2 model ensemble. In particular, ~~models in general~~ 10/15 models agree on increased westward ocean volume transport through the MC during the mid-Pliocene and 5/15 models show decreased volume transport.

4.2 Summary of the PlioMIP2 Model Performance

While MC SST are pronouncedly warmer in the mid-Pliocene, it seems that within the PlioMIP2 model ensemble MC climate is to some extent decoupled from model ECS (Fig. 5). On the other hand, we find that models with a large ECS also produce rather warm mid-Pliocene conditions around the MC; and models with a small ECS show relatively cold conditions (Fig. 5). When using models to predict climate of the MC for different levels of carbon dioxide or changes in earth surface ~~condition~~conditions, it is important to note that the models that best reproduce a recent regional climate of the MC as quantified by a comparison to modern observations are not necessarily the same models as those that produce the best agreement between simulated and reconstructed mid-Pliocene SSTAs (Fig. S3). ~~But at a~~ Yet, at global scale, there is a correlation between model performance on simulating mid-Pliocene and modern climate (Fig. S4). From that point of view, the mid-Pliocene proves to be a real test bed for the skill of models for climate states that strongly differ from the recent one.

Largely, we find agreement between proxy reconstructions of SSTA on the one hand and mid-Pliocene climate simulations on the other hand. At ODP Site 214 ~~some of the~~ a small number of models fall out of the uncertainty range of the reconstruction at the warm end. Yet, we note that ODP214 indeed appears somewhat cool in comparison to nearby SSTA reconstructions in the region. This leaves us with the possibility that the models are not able to capture climate mechanisms that shaped the mid-Pliocene climate recorded at site ODP214. An alternative explanation could be that the discord at this site is to be sought in the proxy data itself or in its interpretation. We note that the model-data comparison is hampered by large uncertainty ranges of reconstructed SSTAs and by limited availability of suitable SSTA reconstructions in the region. This highlights that more studies are necessary that increase availability of MC SSTAs during the mid-Pliocene. On the other hand, we find that the simulated climate in PlioMIP2 has much smaller uncertainty ranges than the reconstructed climate. This is seen from the fact that the spread of simulated SSTAs across the PlioMIP2 model ensemble is much smaller than the uncertainty bars attributed to reconstructions (Fig. 3a). This hints that the proxy reconstructions at the MC are shaped by aspects of regional climate variability that the models fail to capture.

4.3 Model Hierarchy and Clustering

The multimodel ensemble mean (MMM) has frequently been adopted to illustrate models' results. We found the MMM produces less discrepancy than more than half of the PlioMIP2 individual models in both mid-Pliocene ~~climate simulation~~ and preindustrial climate ~~simulation~~ simulations (Fig. S3). In the case of model independence, the model biases will be partially cancelled, which results in the MMM outperforming individual models (Solomon et al., 2007; Knutti et al., 2010). ~~But~~ Yet, some models, such as models adopted in Coupled Model Intercomparison Projects phase 6 (CMIP6)~~are not all independent, they~~, are not fully independent from each other and might have similar biases (Abramowitz et al., 2019). Boé (2018) quantified the relationship between CMIP5 model components replication and proximity of their results, and found there is a clear

relationship at both global and regional scales. Model clustering is a way to study proximity of models results' spatial patterns and to weight models to reduce reduplication of similar biases from the same model family.

As in CMIP6, also PlioMIP2, not all the models are independent from each other. There are models that have been developed from the same source, with shared codes or using different generations of the same components as shown in Table 1. A study from Ho et al. (2016) adopted outputs from 41 CMIP5 models and clustered models according to the concept of "model genealogy" (Knutti et al., 2013b) and found difference between the weighted and unweighted multi-model ensemble mean. Yet, general conclusions from both methods did not change. In this study, we cluster models into groups according to the proximity of their results in simulating SSTAs and precipitation (section 3.4). Although some models used the same ocean component, they turned out to be in different SSTA-based cluster groups, such as CESM2. Descendants of CCSM4, CCSM4-Utr, CCSM4-UoT, CESM1.2, CESM2, NorESM-L and NorESM1-F, are all in cluster 3, except for CESM2 (Fig. 8a). Compared to the other CCSM4 models, CESM2 has updated the POP ocean component not only with respect to the parameterization but also with regard to the use of new schemes (Danabasoglu et al., 2020). Moreover, CCSM4, CESM1.2 and CESM2 have very different atmospheric components. In the study of Pacific Walker Circulation, CCSM4 showed strengthened Walker Circulation, while both CESM1.2 and CESM2 showed weakened Walker Circulation (Feng et al., 2020b). Nearly all the models that include the NEMO ocean component (EC-Earth3.3, IPSLCM5A, IPSLCM5A2, IPSL-CM6A-LR and HadGEM3) except for EC-Earth3.3, appear in the SSTA-based cluster 4 (Fig. 8a). In the analysis of El Niño variability from PlioMIP2 (Oldeman et al., 2021), the 'La Niña-like' mean state model group and the 'El Niño-like' mean state group are not the same as the SSTA-based clusters found in our study. This implies that clustering depends on the region and on the studied physical quantity. In terms of atmospheric component, some models used the same atmosphere component but haven't been clustered into the same group based on precipitation. For example, CCSM4, CCSM4-UoT, CESM1.2 and CESM2 are all in cluster 1, but CCSM4-Utr is not in this group. The two closest models in both SSTA-based and precipitation-based clusters are IPSLCM5A and IPSLCM5A2. They adopted the same atmospheric component and oceanic component, as well as vertical and horizontal resolutions. Compared with the IPSLCM5A, IPSLCM5A2 updated model components and retuned the cloud radiative forcing (Tan et al., 2020), but both models still produce a similar climate signal over the MC. From the discussion above, we conclude that the model configuration can provide to us a reference to cluster models, but even models of the same model family may still produce different climatic signals depending on the analysis region or the studied climate characteristic. These results suggest that there is not always a clear trace of model family apparent via the clustering.

Moreover, the multimodel mean will lead to the loss of climatic signal (Knutti et al., 2010). In our study, there are noticeable variations between spatial anomaly patterns from individual models. By illustrating models' results in cluster groups, climatic signal loss can be reduced, for example the warm anomaly signal in the centre of the Western Pacific Ocean as shown in Fig. 8b.

5 Conclusions

The subaerial Sunda and Sahul shelves and relative high atmospheric CO_2 concentration, combined with other forcings, lead to a different climate of the MC in the mid-Pliocene than in the preindustrial. In line with the global climate, all the 17 PlioMIP2 models (including HadGEM3) show higher SSTs in the mid-Pliocene MC, ranging from +0.43°C to +3.33°C, with a MMM warming by 1.88°C; 13 out of 17 models show fresh water flux ~~(precipitation minus evaporation)~~ P-E increased in the MC, ~~ranging from~~ the anomaly ranging from +0.04 mm/day to +0.50 mm/day. In terms of atmospheric circulation, the easterlies over the western tropical Pacific Ocean show enhanced intensity in the MMM; there is anomalous eastward wind stress over the ocean near ~~the~~ Western Australia. Seawater salinity affects the thermohaline circulation; 14 out of 16 models (MRI-CGCM2.3 is absent here) show a lower SOS in the MC .

Even though the topography of the MC in the mid-Pliocene acts as a barrier for volume transport between the Pacific Ocean and the Indian Ocean compared to the preindustrial, 10 out of 15 models show the ITF intensity increasing by ~~12.2~~5.6% to ~~34.6~~43.8%. ~~Three models do not show apparent changes in intensity. Only~~ CESM2, IPSL-CM6A-LR, COSMOS, MIROCm4 and HadGEM3 ~~and COSMOS~~show a decrease in intensity of the ITF, the amplitude of westward flow is here lowered by ~~38.5~~3.4% ~~and 6.6~~to 39.4%~~, respectively~~. In terms of spatial difference, the MMM shows that the ITF is stronger in the north but weaker in the south in the mid-Pliocene relative to the preindustrial. Moreover, the water mass is mainly transported through the ITF in the ocean above 1000 meters depth in both the preindustrial and the mid-Pliocene. The changes in the volume transport of ITF also mainly occur in the ocean above 1000 meters depth.

The models' performance has also been quantified in this work by comparing the discrepancies between model results and reanalysis data on the one hand and reconstructed data on the other hand. The results imply that models, which reproduce modern climate well, are not always good at simulating the mid-Pliocene climate of the MC according to the proxy reconstructions. ~~But at the global scale~~ At global scale on the other hand, there is a correlation between models' performance on simulating the mid-Pliocene climate and modern climate (see Fig. S5 in ~~appendix~~supplement).

The comparison between individual models and the MMM suggests that the MMM could reproduce the preindustrial SST of the reanalysis better than 13 out of 17 models, and ~~produce~~ show less discrepancy with reconstructed SSTAs than 12 out of 17 models.

There is a big difference in the spatial distribution of anomalies between models. Because ~~similar~~ some models will amplify similar signals, and because some climatic signals from individual models will get lost in the MMM, a new metric MCM has been introduced. It takes model families weight into account, provides a new perspective on ~~ensemble~~ the ensemble of multiple models' results and demonstrates different climate states ~~with~~ by means of clusters. The ~~evaluations~~ evaluation of the MCM ~~show that the MCM also~~ shows that it outperforms 12 out of 17 models in simulating preindustrial climate and shows less or equal discrepancy with reconstructed mid-Pliocene SSTAs than 10 out of 17 models, which suggests that the MCM is a plausible method to show multimodel results.

Code and data availability. The PlioMIP2 model data used in this work is available from the PlioMIP2 database upon request from Alan M. Haywood (a.m.haywood@leeds.ac.uk). PlioMIP2 data from CESM2, EC-Earth3.3, NorESM1-F, IPSLCM6A, GISS2.1G and HadGEM3 can be obtained from the Earth System Grid Federation (https://esgf-node.llnl.gov/search/cmip6/). The boundary conditions for the PlioMIP2 experimental design can be downloaded from https://geology.er.usgs.gov/egpsc/prism/7.2_pliomip2_data.html. Most of the analyses in this paper are processed with NCAR Command Language (NCL), some of the scripts use here have been shared in https://github.com/XinRenn/Xin_MM-cluster.

Author contributions. XR carried out the data process, wrote the manuscript, and led the paper. DJL and EH provided assistance during the whole work. DJL and CS contributed to manuscript writing. AH, AAO, BOB, CJRW, CS, CG, DC, GL, JCT, LES, MAC, MK, MLJB, NT, QZ, RF, WLC, WRP, XL, YK, ZZ and AMH conducted the simulations and provided data. All authors provided comments and contributed to this paper.

Competing interests. The authors declare that they have no conflict of interest.

Acknowledgements. This research is funded by the European Union's Horizon 2020 research and innovation programme under the Marie Skłodowska-Curie grant agreement No 813360 4DREEF and the NERC SWEET grant (grant no. NE/P01903X/1). Wing-Le Chan and Ayako Abe-Ouchi acknowledge funding from JSPS (KAKENHI grant no. 17H06104 and MEXT KAKENHI grant no. 17H06323) and computational resources from the Earth Simulator at JAMSTEC, Yokohama, Japan. Development of GISS-E2.1 was supported by the NASA Modeling, Analysis, and Prediction (MAP) Program. CMIP6 simulations with GISS-E2.1 were made possible by the NASA High-End Computing (HEC) Program through the NASA Center for Climate Simulation (NCCS) at Goddard Space Flight Center. Charles J. R. Williams acknowledges the financial support of the UK Natural Environment Research Council (NERC)-funded SWEET project (research grant no. NE/P01903X/1), as well as funding from the European Research Council (under the European Union's Seventh Framework Programme (FP/2007-868 2013) (ERC grant agreement no. 340923 (TGRES)). GL and CS acknowledge institutional funding at AWI via the research program PACES-II of the Helmholtz Association. CS acknowledges funding via the Helmholtz Climate Initiative REKLIM. MB and AvdH acknowledge support by the program of the Netherlands Earth System Science Centre (NESSC), financially supported by the Ministry of Education, Culture and Science (OCW). Xiangyu Li acknowledge funding from National Natural Science Foundation of China (42005042 and 42275047).

References

Abramowitz, G., Herger, N., Gutmann, E., Hammerling, D., Knutti, R., Leduc, M., Lorenz, R., Pincus, R., and Schmidt, G. A.: ESD Reviews: Model dependence in multi-model climate ensembles: Weighting, sub-selection and out-of-sample testing, Earth System Dynamics, 10, 91–105, https://doi.org/10.5194/ESD-10-91-2019, 2019.

Adler, R. F., Gu, G., Sapiano, M., Wang, J.-J., and Huffman, G. J.: Global Precipitation: Means, Variations and Trends During the Satellite Era (1979–2014), Surveys in Geophysics, 38, 679–699, https://doi.org/10.1007/s10712-017-9416-4, 2017.

Allen, M. R. and Ingram, W. J.: Constraints on future changes in climate and the hydrologic cycle, Nature, 419, 224–232, 2002.

Alley, N. F.: Cainozoic stratigraphy, palaeoenvironments and geological evolution of the Lake Eyre Basin, Palaeogeography, Palaeoclimatology, Palaeoecology, 144, 239–263, https://doi.org/10.1016/S0031-0182(98)00120-5, 1998.

Alory, G., Wijffels, S., and Meyers, G.: Observed temperature trends in the Indian Ocean over 1960–1999 and associated mechanisms, Geophysical Research Letters, 34, L02 606, https://doi.org/10.1029/2006GL028044, 2007.

Andrews, T., Gregory, J. M., and Webb, M. J.: The dependence of radiative forcing and feedback on evolving patterns of surface temperature change in climate models, Journal of Climate, 28, 1630–1648, https://doi.org/10.1175/JCLI-D-14-00545.1, 2015.

Archer, M. and M, W.: RESULTS OF THE RAY E. LEMLEY EXPEDITIONS. I. THE ALLINGHAM FORMATION AND A NEW PLIOCENE VERTEBRATE FAUNA FROM NORTHERN QUEENSLAND., RESULTS OF THE RAY E. LEMLEY EXPEDITIONS. I. THE ALLINGHAM FORMATION AND A NEW PLIOCENE VERTEBRATE FAUNA FROM NORTHERN QUEENSLAND., 1976.

Arias, P., Bellouin, N., Coppola, E., Jones, R., Krinner, G., Marotzke, J., Naik, V., Palmer, M., Plattner, G.-K., Rogelj, J., Rojas, M., Sillmann, J., Storelvmo, T., Thorne, P., Trewin, B., Rao, K. A., Adhikary, B., Allan, R., Armour, K., Bala, G., Barimalala, R., Berge, S., and Zickfeld, K.: Technical Summary., in: Climate Change 2021: The Physical Science Basis.Contribution of Working Group I to the Sixth Assessment Report of the Intergovernmental Panel on Climate Change, edited by Masson-Delmotte, V., Zhai, P., Pirani, A., Connors, S., Péan, C., Berger, S., Caud, N., Chen, Y., Goldfarb, L., Gomis, M., Huang, M., Leitzell, K., Lonnoy, E., Matthews, J., Maycock, T., Waterfield, T., Yelekçi, O., Yu, R., and Zhou, B., p. 3949, Cambridge University Press, https://doi.org/10.1017/9781009157896.002, 2021.

Armour, K. C.: Energy budget constraints on climate sensitivity in light of inconstant climate feedbacks, Nature Climate Change, 7, 331–335, https://doi.org/10.1038/nclimate3278, 2017.

Auer, G., De Vleeschouwer, D., Smith, R. A., Bogus, K., Groeneveld, J., Grunert, P., Castañeda, I. S., Petrick, B., Christensen, B., Fulthorpe, C., Gallagher, S. J., and Henderiks, J.: Timing and Pacing of Indonesian Throughflow Restriction and Its Connection to Late Pliocene Climate Shifts, Paleoceanography and Paleoclimatology, 34, 635–657, https://doi.org/10.1029/2018PA003512, 2019.

Baatsen, M. L. J., von der Heydt, A. S., Kliphuis, M. A., Oldeman, A. M., and Weiffenbach, J. E.: Warm mid-Pliocene conditions without high climate sensitivity: the CCSM4-Utrecht (CESM 1.0.5) contribution to the PlioMIP2, Climate of the Past, 18, 657–679, https://doi.org/10.5194/CP-18-657-2022, 2022.

Boé, J.: Interdependency in Multimodel Climate Projections: Component Replication and Result Similarity, Geophysical Research Letters, 45, 2771–2779, https://doi.org/10.1002/2017GL076829, 2018.

Boucher, O., Servonnat, J., Albright, A. L., Aumont, O., Balkanski, Y., Bastrikov, V., Bekki, S., Bonnet, R., Bony, S., Bopp, L., Braconnot, P., Brockmann, P., Cadule, P., Caubel, A., Cheruy, F., Codron, F., Cozic, A., Cugnet, D., D'Andrea, F., Davini, P., de Lavergne, C., Denvil, S., Deshayes, J., Devilliers, M., Ducharne, A., Dufresne, J. L., Dupont, E., Éthé, C., Fairhead, L., Falletti, L., Flavoni, S., Foujols, M. A., Gardoll, S., Gastineau, G., Ghattas, J., Grandpeix, J. Y., Guenet, B., Guez, Lionel, E., Guilyardi, E., Guimberteau, M., Hauglustaine, D., Hourdin, F., Idelkadi, A., Joussaume, S., Kageyama, M., Khodri, M., Krinner, G., Lebas, N., Levavasseur, G., Lévy, C., Li, L., Lott, F.,

Lurton, T., Luyssaert, S., Madec, G., Madeleine, J. B., Maignan, F., Marchand, M., Marti, O., Mellul, L., Meurdesoif, Y., Mignot, J., Musat, I., Ottlé, C., Peylin, P., Planton, Y., Polcher, J., Rio, C., Rochetin, N., Rousset, C., Sepulchre, P., Sima, A., Swingedouw, D., Thiéblemont, R., Traore, A. K., Vancoppenolle, M., Vial, J., Vialard, J., Viovy, N., and Vuichard, N.: Presentation and Evaluation of the IPSL-CM6A-LR Climate Model, Journal of Advances in Modeling Earth Systems, 12, e2019MS002 010, https://doi.org/10.1029/2019MS002010, 2020.

Brierley, C. M.: Interannual climate variability seen in the Pliocene Model Intercomparison Project, Climate of the Past, 11, 605–618, https://doi.org/10.5194/cp-11-605-2015, 2015.

Brierley, C. M. and Fedorov, A. V.: Comparing the impacts of Miocene–Pliocene changes in inter-ocean gateways on climate: Central American Seaway, Bering Strait, and Indonesia, Earth and Planetary Science Letters, 444, 116–130, https://doi.org/10.1016/j.epsl.2016.03.010, 2016.

Burke, K. D., Williams, J. W., Chandler, M. A., Haywood, A. M., Lunt, D. J., and Otto-Bliesner, B. L.: Pliocene and Eocene provide best analogs for near-future climates, Proceedings of the National Academy of Sciences, 115, 13 288–13 293, https://doi.org/10.1073/pnas.1809600115, 2018.

Byrne, D., Garcia-Soto, C., Hamilton, G., Leuliette, E., Campos, E., Durack, P. J., Manzella, G. M., Tadokoro, K., Schmitt, R. W., Arkin, P., Bryden, H., Nurse, L., Milliman, J., Inniss, L., and Bernal, P.: Chapter 4. The Ocean's Role in the Hydrological Cycle, chap. 4, pp. 91 – 104, Cambridge University Press, Cambridge, UK, and New York, NY, USA, 582 pp., 2016.

Cane, M. A. and Molnar, P.: Closing of the Indonesian seaway as a precursor to east African aridification around 3–4 million years ago, Nature, 411, 157–162, https://doi.org/10.1038/35075500, 2001.

Ceppi, P. and Gregory, J. M.: Relationship of tropospheric stability to climate sensitivity and Earth's observed radiation budget, Proceedings of the National Academy of Sciences of the United States of America, 114, 13 126–13 131, https://doi.org/10.1073/pnas.1714308114, 2017.

Chan, W.-L. and Abe-Ouchi, A.: Pliocene Model Intercomparison Project (PlioMIP2) simulations using the Model for Interdisciplinary Research on Climate (MIROC4m), Climate of the Past, 16, 1523–1545, https://doi.org/10.5194/cp-16-1523-2020, 2020.

Chandan, D. and Peltier, W. R.: Regional and global climate for the mid-Pliocene using the University of Toronto version of CCSM4 and PlioMIP2 boundary conditions, Climate of the Past, 13, 919–942, https://doi.org/10.5194/cp-13-919-2017, 2017.

Christensen, B. A., Renema, W., Henderiks, J., De Vleeschouwer, D., Groeneveld, J., Castañeda, I. S., Reuning, L., Bogus, K., Auer, G., Ishiwa, T., McHugh, C. M., Gallagher, S. J., Fulthorpe, C. S., Mamo, B. L., Kominz, M. A., McGregor, H. V., Petrick, B. F., Takayanagi, H., Levin, E., Korpanty, C. A., Potts, D. C., Baranwal, S., Franco, D. R., Gurnis, M., Haller, C., He, Y., Himmler, T., Iwatani, H., Jatiningrum, R. S., Lee, E. Y., Rastigar, A., and Zhang, W.: Indonesian Throughflow drove Australian climate from humid Pliocene to arid Pleistocene, Geophysical Research Letters, 44, 6914–6925, https://doi.org/10.1002/2017GL072977, 2017.

Corvec, S. and Fletcher, C. G.: Changes to the tropical circulation in the mid-Pliocene and their implications for future climate, Climate of the Past, 13, 135–147, https://doi.org/10.5194/cp-13-135-2017, 2017.

Curry, W., Thunell, R., and Honjo, S.: Seasonal changes in the isotopic composition of planktonic foraminifera collected in Panama Basin sediment traps, Earth and Planetary Science Letters, 64, 33–43, https://doi.org/10.1016/0012-821X(83)90050-X, 1983.

Danabasoglu, G., Bates, S. C., Briegleb, B. P., Jayne, S. R., Jochum, M., Large, W. G., Peacock, S., and Yeager, S. G.: The CCSM4 Ocean Component, Journal of Climate, 25, 1361–1389, https://doi.org/10.1175/JCLI-D-11-00091.1, 2012.

Danabasoglu, G., Lamarque, J. F., Bacmeister, J., Bailey, D. A., DuVivier, A. K., Edwards, J., Emmons, L. K., Fasullo, J., Garcia, R., Gettelman, A., Hannay, C., Holland, M. M., Large, W. G., Lauritzen, P. H., Lawrence, D. M., Lenaerts, J. T., Lindsay, K., Lipscomb, W. H., Mills, M. J., Neale, R., Oleson, K. W., Otto-Bliesner, B., Phillips, A. S., Sacks, W., Tilmes, S., van Kampenhout, L., Vertenstein,

M., Bertini, A., Dennis, J., Deser, C., Fischer, C., Fox-Kemper, B., Kay, J. E., Kinnison, D., Kushner, P. J., Larson, V. E., Long, M. C., Mickelson, S., Moore, J. K., Nienhouse, E., Polvani, L., Rasch, P. J., and Strand, W. G.: The Community Earth System Model Version 2 (CESM2), Journal of Advances in Modeling Earth Systems, 12, e2019MS001 916, https://doi.org/10.1029/2019MS001916, 2020.

Dayem, K. E., Noone, D. C., and Molnar, P.: Tropical western Pacific warm pool and maritime continent precipitation rates and their contrasting relationships with the Walker Circulation, Journal of Geophysical Research, 112, D06 101, https://doi.org/10.1029/2006JD007870, 2007.

Dong, Y., Armour, K. C., Zelinka, M. D., Proistosescu, C., Battisti, D. S., Zhou, C., and Andrews, T.: Intermodel spread in the pattern effect and its contribution to climate sensitivity in CMIP5 and CMIP6 models, Journal of Climate, 33, 7755–7775, https://doi.org/10.1175/JCLI-D-19-1011.1, 2020.

Dowsett, H., Robinson, M., Haywood, A., Salzmann, U., Hill, D., Sohl, L., Chandler, M., Williams, M., Foley, K., and Stoll, D.: The PRISM3D paleoenvironmental reconstruction, Stratigraphy, 2010.

Dowsett, H., Dolan, A., Rowley, D., Moucha, R., Forte, A. M., Mitrovica, J. X., Pound, M., Salzmann, U., Robinson, M., Chandler, M., Foley, K., and Haywood, A.: The PRISM4 (mid-Piacenzian) paleoenvironmental reconstruction, Climate of the Past, 12, 1519–1538, https://doi.org/10.5194/cp-12-1519-2016, 2016.

Dowsett, H. J., Robinson, M. M., Stoll, D. K., Foley, K. M., Johnson, A. L. A., Williams, M., and Riesselman, C. R.: The PRISM (Pliocene palaeoclimate) reconstruction: time for a paradigm shift, Philosophical Transactions of the Royal Society A: Mathematical, Physical and Engineering Sciences, 371, 20120 524, https://doi.org/10.1098/rsta.2012.0524, 2013.

Drushka, K., Sprintall, J., Gille, S. T., and Brodjonegoro, I.: Vertical Structure of Kelvin Waves in the Indonesian Throughflow Exit Passages, Journal of Physical Oceanography, 40, 1965–1987, https://doi.org/10.1175/2010JPO4380.1, 2010.

Fairbanks, R. G., Wiebe, P. H., and Bé, A. W. H.: Vertical Distribution and Isotopic Composition of Living Planktonic Foraminifera in the Western North Atlantic, Science, 207, 61–63, https://doi.org/10.1126/science.207.4426.61, 1980.

Fedorov, A. V., Burls, N. J., Lawrence, K. T., and Peterson, L. C.: Tightly linked zonal and meridional sea surface temperature gradients over the past five million years, Nature Geoscience 2015 8:12, 8, 975–980, https://doi.org/10.1038/ngeo2577, 2015.

Feng, M., Zhang, N., Liu, Q., and Wijffels, S.: The Indonesian throughflow, its variability and centennial change, https://doi.org/10.1186/s40562-018-0102-2, 2018.

Feng, R., Otto-Bliesner, B. L., Brady, E. C., and Rosenbloom, N.: Increased Climate Response and Earth System Sensitivity From CCSM4 to CESM2 in Mid-Pliocene Simulations, Journal of Advances in Modeling Earth Systems, 12, e2019MS002 033, https://doi.org/10.1029/2019MS002033, 2020a.

Feng, R., Otto-Bliesner, B. L., Brady, E. C., and Rosenbloom, N.: Increased Climate Response and Earth System Sensitivity From CCSM4 to CESM2 in Mid-Pliocene Simulations, Journal of Advances in Modeling Earth Systems, 12, 0–2, https://doi.org/10.1029/2019MS002033, 2020b.

Feng, R., Bhattacharya, T., Otto-Bliesner, B. L., Brady, E. C., Haywood, A. M., Tindall, J. C., Hunter, S. J., Abe-Ouchi, A., Chan, W. L., Kageyama, M., Contoux, C., Guo, C., Li, X., Lohmann, G., Stepanek, C., Tan, N., Zhang, Q., Zhang, Z., Han, Z., Williams, C. J., Lunt, D. J., Dowsett, H. J., Chandan, D., and Peltier, W. R.: Past terrestrial hydroclimate sensitivity controlled by Earth system feedbacks, Nature Communications 2022 13:1, 13, 1–11, https://doi.org/10.1038/s41467-022-28814-7, 2022.

Gordon, A.: Oceanography of the Indonesian Seas and Their Throughflow, Oceanography, 18, 14–27, https://doi.org/10.5670/oceanog.2005.01, 2005a.

Gordon, A., Sprintall, J., Van Aken, H., Susanto, D., Wijffels, S., Molcard, R., Ffield, A., Pranowo, W., and Wirasantosa, S.: The Indonesian throughflow during 2004–2006 as observed by the INSTANT program, Dynamics of Atmospheres and Oceans, 50, 115–128, https://doi.org/10.1016/j.dynatmoce.2009.12.002, 2010.

810 Gordon, A. L.: Oceanography of the Indonesian seas and their throughflow, Oceanography, 18, 15–27, https://doi.org/10.5670/oceanog.2005.01, 2005b.

Gordon, A. L. and Doherty, L.: The Indonesian Throughflow, its characteristics, drivers, and impact on the Indian Ocean, Tech. rep.

Gregory, J. M. and Andrews, T.: Variation in climate sensitivity and feedback parameters during the historical period, Geophysical Research Letters, 43, 3911–3920, https://doi.org/10.1002/2016GL068406, 2016.

815 Gutiérrez, J.M., R. J., G.T. Narisma, L.M. Alves, M. Amjad, I.V. Gorodetskaya, M. Grose, N.A.B. Klutse, S. Krakovska, J. Li, D. Martínez-Castro, L.O. Mearns, S.H. Mernild, T. Ngo-Duc, B. van den Hurk, and Yoon, J.-H.: Ocean, Cryosphere and Sea Level Change. Contribution of Working Group I to the Sixth Assessment Report of the Intergovernmental Panel on Climate Change, in: Climate Change 2021: The Physical Science Basis, p. 3949, Megan Kirchmeier-Young, https://doi.org/10.1017/9781009157896.021, 2021.

Han, Z., Zhang, Q., Li, Q., Feng, R., Haywood, A. M., Tindall, J. C., Hunter, S. J., Otto-Bliesner, B. L., Brady, E. C., Rosenbloom, N.,
820 Zhang, Z., Li, X., Guo, C., Nisancioglu, K. H., Stepanek, C., Lohmann, G., Sohl, L. E., Chandler, M. A., Tan, N., Ramstein, G., Baatsen, M. L., Von Der Heydt, A. S., Chandan, D., Peltier, W. R., Williams, C. J., Lunt, D. J., Cheng, J., Wen, Q., and Burls, N. J.: Evaluating the large-scale hydrological cycle response within the Pliocene Model Intercomparison Project Phase 2 (PlioMIP2) ensemble, Climate of the Past, 17, 2537–2558, https://doi.org/10.5194/cp-17-2537-2021, 2021.

Haywood, A. M., Dowsett, H. J., Otto-Bliesner, B., Chandler, M. A., Dolan, A. M., Hill, D. J., Lunt, D. J., Robinson, M. M., Rosenbloom,
825 N., Salzmann, U., and Sohl, L. E.: Pliocene Model Intercomparison Project (PlioMIP): experimental design and boundary conditions (Experiment 1), Geoscientific Model Development, 3, 227–242, https://doi.org/10.5194/gmd-3-227-2010, 2010.

Haywood, A. M., Dowsett, H. J., Robinson, M. M., Stoll, D. K., Dolan, A. M., Lunt, D. J., Otto-Bliesner, B., and Chandler, M. A.: Pliocene Model Intercomparison Project (PlioMIP): experimental design and boundary conditions (Experiment 2), Geoscientific Model Development, 4, 571–577, https://doi.org/10.5194/gmd-4-571-2011, 2011.

830 Haywood, A. M., Hill, D. J., Dolan, A. M., Otto-Bliesner, B. L., Bragg, F., Chan, W. L., Chandler, M. A., Contoux, C., Dowsett, H. J., Jost, A., Kamae, Y., Lohmann, G., Lunt, D. J., Abe-Ouchi, A., Pickering, S. J., Ramstein, G., Rosenbloom, N. A., Salzmann, U., Sohl, L., Stepanek, C., Ueda, H., Yan, Q., and Zhang, Z.: Large-scale features of Pliocene climate: Results from the Pliocene Model Intercomparison Project, Climate of the Past, 9, 191–209, https://doi.org/10.5194/cp-9-191-2013, 2013.

Haywood, A. M., Dowsett, H. J., and Dolan, A. M.: Integrating geological archives and climate models for the mid-Pliocene warm period,
835 Nature Communications, 6, 1–14, https://doi.org/10.1038/ncomms10646, 2016a.

Haywood, A. M., Dowsett, H. J., Dolan, A. M., Rowley, D., Abe-Ouchi, A., Otto-Bliesner, B., Chandler, M. A., Hunter, S. J., Lunt, D. J., Pound, M., and Salzmann, U.: The Pliocene Model Intercomparison Project (PlioMIP) Phase 2: scientific objectives and experimental design, Climate of the Past, 12, 663–675, https://doi.org/10.5194/cp-12-663-2016, 2016b.

Haywood, A. M., Tindall, J. C., Dowsett, H. J., Dolan, A. M., Foley, K. M., Hunter, S. J., Hill, D. J., Chan, W. L., Abe-Ouchi, A., Stepanek,
840 C., Lohmann, G., Chandan, D., Richard Peltier, W., Tan, N., Contoux, C., Ramstein, G., Li, X., Zhang, Z., Guo, C., Nisancioglu, K. H., Zhang, Q., Li, Q., Kamae, Y., Chandler, M. A., Sohl, L. E., Otto-Bliesner, B. L., Feng, R., Brady, E. C., Von Der Heydt, A. S., Baatsen, M. L., and Lunt, D. J.: The Pliocene Model Intercomparison Project Phase 2: Large-scale climate features and climate sensitivity, Climate of the Past, 16, 2095–2123, https://doi.org/10.5194/cp-16-2095-2020, 2020.

Hertzberg, J. E. and Schmidt, M. W.: Refining Globigerinoides ruber Mg/Ca paleothermometry in the Atlantic Ocean, Earth and Planetary
845   Science Letters, 383, 123–133, https://doi.org/10.1016/j.epsl.2013.09.044, 2013.

Ho, J. T., Thompson, J. R., and Brierley, C.: Projections of hydrology in the Tocantins-Araguaia Basin, Brazil: uncertainty assessment using
the CMIP5 ensemble, https://doi.org/10.1080/02626667.2015.1057513, 61, 551–567, https://doi.org/10.1080/02626667.2015.1057513,
2016.

Hönisch, B., Allen, K. A., Lea, D. W., Spero, H. J., Eggins, S. M., Arbuszewski, J., DeMenocal, P., Rosenthal, Y., Russell, A. D., and Elder-
850   field, H.: The influence of salinity on Mg/Ca in planktic foraminifers – Evidence from cultures, core-top sediments and complementary
$\delta18O$, Geochimica et Cosmochimica Acta, 121, 196–213, https://doi.org/10.1016/j.gca.2013.07.028, 2013.

Hourdin, F., Grandpeix, J. Y., Rio, C., Bony, S., Jam, A., Cheruy, F., Rochetin, N., Fairhead, L., Idelkadi, A., Musat, I., Dufresne, J. L.,
Lahellec, A., Lefebvre, M. P., and Roehrig, R.: LMDZ5B: The atmospheric component of the IPSL climate model with revisited param-
eterizations for clouds and convection, Climate Dynamics, 40, 2193–2222, https://doi.org/10.1007/S00382-012-1343-Y/FIGURES/23,
855   2013.

Hourdin, F., Rio, C., Grandpeix, J. Y., Madeleine, J. B., Cheruy, F., Rochetin, N., Jam, A., Musat, I., Idelkadi, A., Fairhead, L., Fou-
jols, M. A., Mellul, L., Traore, A. K., Dufresne, J. L., Boucher, O., Lefebvre, M. P., Millour, E., Vignon, E., Jouhaud, J., Diallo,
F. B., Lott, F., Gastineau, G., Caubel, A., Meurdesoif, Y., and Ghattas, J.: LMDZ6A: The Atmospheric Component of the IPSL
Climate Model With Improved and Better Tuned Physics, Journal of Advances in Modeling Earth Systems, 12, e2019MS001 892,
860   https://doi.org/10.1029/2019MS001892, 2020.

Hunter, S. J., Haywood, A. M., Dolan, A. M., and Tindall, J. C.: The HadCM3 contribution to PlioMIP phase 2, Climate of the Past, 15,
1691–1713, https://doi.org/10.5194/cp-15-1691-2019, 2019.

Iturbide, M., Fernández, J., Gutiérrez, J. M., Bedia, J., Cimadevilla, E., Díez-Sierra, J., Manzanas, R., Casanueva, A., Baño-Medina, J.,
Milovac, J., Herrera, S., Cofiño, A. S., San Martín, D., García-Díez, M., Hauser, M., Huard, D., and Yelekci, Ö.: Repository supporting
865   the implementation of FAIR principles in the IPCC-WGI Atlas, https://doi.org/10.5281/ZENODO.5171760, 2021.

Jian, Z., Zhao, Q., Cheng, X., Wang, J., Wang, P., and Su, X.: Pliocene–Pleistocene stable isotope and paleoceanographic changes in the north-
ern South China Sea, Palaeogeography, Palaeoclimatology, Palaeoecology, 193, 425–442, https://doi.org/10.1016/S0031-0182(03)00259-
1, 2003.

Kageyama, M., Harrison, S. P., Kapsch, M.-L., Lofverstrom, M., Lora, J. M., Mikolajewicz, U., Sherriff-Tadano, S., Vadsaria, T., Abe-Ouchi,
870   A., Bouttes, N., Chandan, D., Gregoire, L. J., Ivanovic, R. F., Izumi, K., LeGrande, A. N., Lhardy, F., Lohmann, G., Morozova, P. A.,
Ohgaito, R., Paul, A., Peltier, W. R., Poulsen, C. J., Quiquet, A., Roche, D. M., Shi, X., Tierney, J. E., Valdes, P. J., Volodin, E., and Zhu,
J.: The PMIP4 Last Glacial Maximum experiments: preliminary results and comparison with the PMIP3 simulations, Climate of the Past,
17, 1065–1089, https://doi.org/10.5194/cp-17-1065-2021, 2021.

Kamae, Y., Yoshida, K., and Ueda, H.: Sensitivity of Pliocene climate simulations in MRI-CGCM2.3 to respective boundary conditions,
875   Climate of the Past, 12, 1619–1634, https://doi.org/10.5194/cp-12-1619-2016, 2016.

Karas, C., Nürnberg, D., Gupta, A. K., Tiedemann, R., Mohan, K., and Bickert, T.: Mid-Pliocene climate change amplified by a switch in
Indonesian subsurface throughflow, Nature Geoscience, 2, 434–438, https://doi.org/10.1038/ngeo520, 2009.

Kelley, M., Schmidt, G. A., Nazarenko, L. S., Bauer, S. E., Ruedy, R., Russell, G. L., Ackerman, A. S., Aleinov, I., Bauer, M., Bleck, R.,
Canuto, V., Cesana, G., Cheng, Y., Clune, T. L., Cook, B. I., Cruz, C. A., Del Genio, A. D., Elsaesser, G. S., Faluvegi, G., Kiang, N. Y.,
880   Kim, D., Lacis, A. A., Leboissetier, A., LeGrande, A. N., Lo, K. K., Marshall, J., Matthews, E. E., McDermid, S., Mezuman, K., Miller,
R. L., Murray, L. T., Oinas, V., Orbe, C., García-Pando, C. P., Perlwitz, J. P., Puma, M. J., Rind, D., Romanou, A., Shindell, D. T., Sun,

S., Tausnev, N., Tsigaridis, K., Tselioudis, G., Weng, E., Wu, J., and Yao, M. S.: GISS-E2.1: Configurations and Climatology, Journal of Advances in Modeling Earth Systems, 12, e2019MS002 025, https://doi.org/10.1029/2019MS002025, 2020.

Kershaw, A. P. and Sluiter, I. R.: Late Cenozoic pollen spectra from the Atherton Tableland, north-eastern Australia, Australian Journal of Botany, 30, 279–295, https://doi.org/10.1071/BT9820279, 1982.

Knutti, R., Furrer, R., Tebaldi, C., Cermak, J., and Meehl, G. A.: Challenges in combining projections from multiple climate models, Journal of Climate, 23, 2739–2758, https://doi.org/10.1175/2009JCLI3361.1, 2010.

Knutti, R., Masson, D., and Gettelman, A.: Climate model genealogy: Generation CMIP5 and how we got there, Geophysical Research Letters, 40, 1194–1199, https://doi.org/10.1002/GRL.50256, 2013a.

Knutti, R., Masson, D., and Gettelman, A.: Climate model genealogy: Generation CMIP5 and how we got there, Geophysical Research Letters, 40, 1194–1199, https://doi.org/10.1002/GRL.50256, 2013b.

Lee, T., Fukumori, I., Menemenlis, D., Xing, Z., and Fu, L.-L.: Effects of the Indonesian Throughflow on the Pacific and Indian Oceans, Journal of Physical Oceanography, 32, 1404–1429, https://doi.org/10.1175/1520-0485(2002)032<1404:EOTITO>2.0.CO;2, 2002.

Li, B., Wang, J., Huang, B., Li, Q., Jian, Z., Zhao, Q., Su, X., and Wang, P.: South China Sea surface water evolution over the last 12 Myr: A south-north comparison from Ocean Drilling Program Sites 1143 and 1146, Paleoceanography, 19, https://doi.org/10.1029/2003PA000906, 2004.

Li, M., Gordon, A. L., Wei, J., Gruenburg, L. K., and Jiang, G.: Multi-decadal timeseries of the Indonesian throughflow, Dynamics of Atmospheres and Oceans, 81, 84–95, https://doi.org/10.1016/j.dynatmoce.2018.02.001, 2018a.

Li, X., Guo, C., Zhang, Z., Otterå, O. H., and Zhang, R.: PlioMIP2 simulations with NorESM-L and NorESM1-F, pp. 183–197, 2020.

Li, Y., Yang, S., Deng, Y., Hu, X., and Cai, M.: A process-level attribution of the annual cycle of surface temperature over the Maritime Continent, Climate Dynamics, 51, 2759–2772, https://doi.org/10.1007/s00382-017-4043-9, 2018b.

Macphail, M. K.: Late Neogene Climates in Australia: Fossil Pollen- and Spore-based Estimates in Retrospect and Prospect, Australian Journal of Botany, 45, 425–464, https://doi.org/10.1071/BT96052, 1997.

Macphail, M. K., Alley, N. F., TRUSWELL, E. M., and SLUITER, I. R. K.: Early Tertiary vegetation: evidence from spores and pollen, pp. 189–261, University of Adelaide Press, http://www.jstor.org/stable/10.20851/j.ctt1sq5wrv.14, 1994.

Madec, G.: NEMO ocean engine, vol. 27, http://www.nemo-ocean.eu/About-NEMO/Reference-manualshttp://eprints.soton.ac.uk/64324/, 2012.

Markwick, P. J.: The palaeogeographic and palaeoclimatic significance of climate proxies for data-model comparisons, Geological Society Special Publication, pp. 251–312, https://doi.org/10.1144/tms002.13, 2007.

Marsland, S. J., Haak, H., Jungclaus, J. H., Latif, M., and Röske, F.: The Max-Planck-Institute global ocean/sea ice model with orthogonal curvilinear coordinates, Ocean Modelling, 5, 91–127, https://doi.org/10.1016/S1463-5003(02)00015-X, 2003.

Martin, H. A.: Cenozoic climatic change and the development of the arid vegetation in Australia, Journal of Arid Environments, 66, 533–563, https://doi.org/10.1016/J.JARIDENV.2006.01.009, 2006.

Martin, H. A. and McMinn, A.: Late Cainozoic Vegetation History of North-Western Australia, From the Palynology of a Deep Sea Core (ODP Site 765), Australian Journal of Botany, 42, 95–102, https://doi.org/10.1071/BT9940095, 1994.

Martin Helene, A. and Andrew, M.: Palynology of Sites 815 and 823; the Neogene vegetation history of coastal northeastern Australia, Proceedings of the Ocean DrillingProgram, Scientific Results 133: 115-128, 133, 115–128, https://eurekamag.com/research/019/674/019674099.php, 1993.

Mastrandrea, M. D., Field, C. B., Stocker, T. F., Edenhofer, O., Ebi, K. L., Frame, D. J., Held, H., Kriegler, E., Mach, K. J., Matschoss, P. R., Plattner, G.-K., Yohe, G. W., and Zwiers, F. W.: Guidance Note for Lead Authors of the IPCC Fifth Assessment Report on Consistent Treatment of Uncertainties, Tech. rep., http://www.ipcc.ch, 2010.

McClymont, E. L., Ford, H. L., Ho, S. L., Tindall, J. C., Haywood, A. M., Alonso-Garcia, M., Bailey, I., Berke, M. A., Littler, K., Patterson, M. O., Petrick, B., Peterse, F., Ravelo, A. C., Risebrobakken, B., De Schepper, S., Swann, G. E. A., Thirumalai, K., Tierney, J. E., van der Weijst, C., White, S., Abe-Ouchi, A., Baatsen, M. L. J., Brady, E. C., Chan, W.-L., Chandan, D., Feng, R., Guo, C., von der Heydt, A. S., Hunter, S., Li, X., Lohmann, G., Nisancioglu, K. H., Otto-Bliesner, B. L., Peltier, W. R., Stepanek, C., and Zhang, Z.: Lessons from a high CO2 world: an ocean view from ∼ 3 million years ago, Climate of the Past, 16, 1599–1615, https://doi.org/10.5194/cp-16-1599-2020, 2020.

Neale, R. and Slingo, J.: The Maritime Continent and its role in the global climate: A GCM study, Journal of Climate, 16, 834–848, https://doi.org/10.1175/1520-0442(2003)016<0834:TMCAIR>2.0.CO;2, 2003.

Neale, R. B., Richter, J. H., Conley, A. J., Park, S., Lauritzen, P. H., Gettelman, A., and Williamson, D. L.: Description of the NCAR Community Atmosphere Model (CAM 4.0), Tech. Rep. April, https://www.researchgate.net/publication/224017879_Description_of_the_Community_Atmosphere_Model_CAM_40, 2010.

O'Brien, C. L., Foster, G. L., Martínez-Botí, M. A., Abell, R., Rae, J. W., and Pancost, R. D.: High sea surface temperatures in tropical warm pools during the Pliocene, Nature Geoscience 2014 7:8, 7, 606–611, https://doi.org/10.1038/ngeo2194, 2014.

Oldeman, A. M., Baatsen, M. L. J., von der Heydt, A. S., Dijkstra, H. A., Tindall, J. C., Abe-Ouchi, A., Booth, A. R., Brady, E. C., Chan, W.-L., Chandan, D., Chandler, M. A., Contoux, C., Feng, R., Guo, C., Haywood, A. M., Hunter, S. J., Kamae, Y., Li, Q., Li, X., Lohmann, G., Lunt, D. J., Nisancioglu, K. H., Otto-Bliesner, B. L., Peltier, W. R., Pontes, G. M., Ramstein, G., Sohl, L. E., Stepanek, C., Tan, N., Zhang, Q., Zhang, Z., Wainer, I., and Williams, C. J. R.: Reduced El Niño variability in the mid-Pliocene according to the PlioMIP2 ensemble, Climate of the Past, 17, 2427–2450, https://doi.org/10.5194/cp-17-2427-2021, 2021.

Owen, R. B. and Utha-aroon, C.: Diatomaceous sedimentation in the Tertiary Lampang Basin, Northern Thailand, Journal of Paleolimnology, 22, 81–95, https://doi.org/10.1023/A:1008033813344/METRICS, 1999.

Peltier, W. R. and Vettoretti, G.: Dansgaard-Oeschger oscillations predicted in a comprehensive model of glacial climate: A "kicked" salt oscillator in the Atlantic, Geophysical Research Letters, 41, 7306–7313, https://doi.org/10.1002/2014GL061413, 2014.

Pontes, G., Taschetto, A., Seng Gupta, A., Santoso, A., Wainer, I., Haywood, A., Chan, W.-L., Abe-Ouchi, A., Stepanek, C., Lohmann, G., Hunter, S. J., Tindall, J. C., Chandler, M. A., Sohl, L. E., Peltier, W. R., Chandan, D., Kamae, Y., Nisancioglu, K. H., Zhang, Z., Contoux, C., Tan, N., Zhang, Q., Otto-Bliesner, B. L., Brady, E. C., Feng, R., von der Heydt, A. S., Baatsen, M. L. J., and Oldeman, A. M.: Northward ITCZ shift drives reduced ENSO activity in the Mid-Pliocene Warm Period, Nature Geoscience, Preprint, https://doi.org/10.21203/RS.3.RS-402220/V1, 2021.

Pujiana, K., Gordon, A. L., and Sprintall, J.: Intraseasonal Kelvin wave in Makassar Strait, Journal of Geophysical Research: Oceans, 118, 2023–2034, https://doi.org/10.1002/jgrc.20069, 2013.

R Williams, C. J., Lunt, D. J., Salzmann, U., Reichgelt, T., Inglis, G. N., Greenwood, D. R., Chan, W.-L., Abe-Ouchi, A., Donnadieu, Y., Hutchinson, D. K., de Boer, A. M., Ladant, J.-B., Morozova, P. A., Niezgodzki, I., Knorr, G., Steinig, S., Zhang, Z., Zhu, J., Huber, M., Otto-Bliesner, B. L., and R Williams, C. J.: African Hydroclimate During the Early Eocene From the DeepMIP Simulations, Paleoceanography and Paleoclimatology, 37, e2022PA004 419, https://doi.org/10.1029/2022PA004419, 2022.

RAMAGE, C. S.: ROLE OF A TROPICAL "MARITIME CONTINENT" IN THE ATMOSPHERIC CIRCULATION 1, Monthly Weather Review, 96, 365–370, https://doi.org/10.1175/1520-0493(1968)096<0365:ROATMC>2.0.CO;2, 1968.

Ravelo, A. C. and Fairbanks, R. G.: Oxygen Isotopic Composition of Multiple Species of Planktonic Foraminifera: Recorders of the Modern Photic Zone Temperature Gradient, Paleoceanography, 7, 815–831, https://doi.org/10.1029/92PA02092, 1992.

Rayner, N. A.: Global analyses of sea surface temperature, sea ice, and night marine air temperature since the late nineteenth century, Journal of Geophysical Research, 108, 4407, https://doi.org/10.1029/2002JD002670, 2003.

Roeckner, E., Bäuml, G., Bonaventura, L., Brokopf, R., Esch, M., Giorgetta, M., Hagemann, S., Kirchner, I., Kornblueh, L., Rhodin, A., Schlese, U., Schulzweida, U., and Tompkins, A.: The atmospheric general circulation model ECHAM5: Part 1: Model description, MPI Report, pp. 1–140, www.mpimet.mpg.dehttp://en.scientificcommons.org/8586047, 2003.

Salzmann, U., Haywood, A., and Lunt, D.: The past is a guide to the future? Comparing Middle Pliocene vegetation with predicted biome distributions for the twenty-first century, Philosophical Transactions of the Royal Society A: Mathematical, Physical and Engineering Sciences, 367, 189–204, https://doi.org/10.1098/rsta.2008.0200, 2009.

Sarathchandraprasad, T., Tiwari, M., and Behera, P.: South Asian Summer Monsoon precipitation variability during late Pliocene: Role of Indonesian Throughflow, Palaeogeography, Palaeoclimatology, Palaeoecology, 574, 110 447, https://doi.org/10.1016/j.palaeo.2021.110447, 2021.

Sen Gupta, A., Ganachaud, A., McGregor, S., Brown, J. N., and Muir, L.: Drivers of the projected changes to the Pacific Ocean equatorial circulation, Geophysical Research Letters, 39, n/a–n/a, https://doi.org/10.1029/2012GL051447, 2012.

Sen Gupta, A., McGregor, S., Van Sebille, E., Ganachaud, A., Brown, J. N., and Santoso, A.: Future changes to the Indonesian Throughflow and Pacific circulation: The differing role of wind and deep circulation changes, Geophysical Research Letters, 43, 1669–1678, https://doi.org/10.1002/2016GL067757, 2016.

Sepulchre, P., Caubel, A., Ladant, J.-B., Bopp, L., Boucher, O., Braconnot, P., Brockmann, P., Cozic, A., Donnadieu, Y., Dufresne, J.-L., Estella-Perez, V., Ethé, C., Fluteau, F., Foujols, M.-A., Gastineau, G., Ghattas, J., Hauglustaine, D., Hourdin, F., Kageyama, M., Khodri, M., Marti, O., Meurdesoif, Y., Mignot, J., Sarr, A.-C., Servonnat, J., Swingedouw, D., Szopa, S., and Tardif, D.: IPSL-CM5A2 – an Earth system model designed for multi-millennial climate simulations, Geoscientific Model Development, 13, 3011–3053, https://doi.org/10.5194/gmd-13-3011-2020, 2020.

Shilimkar, V., Abe, H., Roxy, M. K., and Tanimoto, Y.: Projected future changes in the contribution of Indo-Pacific sea surface height variability to the Indonesian throughflow, Journal of Oceanography, 78, 337–352, https://doi.org/10.1007/s10872-022-00641-w, 2022.

Sierra, J. P., Arias, P. A., Vieira, S. C., and Agudelo, J.: How well do CMIP5 models simulate the low-level jet in western Colombia?, Climate Dynamics 2017 51:5, 51, 2247–2265, https://doi.org/10.1007/S00382-017-4010-5, 2017.

Smith, R. A., Castañeda, I. S., Groeneveld, J., De Vleeschouwer, D., Henderiks, J., Christensen, B. A., Renema, W., Auer, G., Bogus, K., Gallagher, S. J., and Fulthorpe, C. S.: Retracted: Plio-Pleistocene Indonesian Throughflow Variability Drove Eastern Indian Ocean Sea Surface Temperatures, Paleoceanography and Paleoclimatology, 35, e2020PA003 872, https://doi.org/10.1029/2020PA003872, 2020.

Solomon, S., Qin, D., Manning, M., Chen, Z., Marquis, M., Averyt, K., Tignor, M., and Miller, H.: Contribution of Working Group I to the Fourth Assessment Report of the Intergovernmental Panel on Climate Change, p. 996, Cambridge University Press, Cambridge, United Kingdom and New York, NY, USA, https://www.ipcc.ch/report/ar4/wg1/http://www.ipcc.ch/publications_and_data/ar4/wg1/en/ch5s5-es.html, 2007.

Sprintall, J. and Révelard, A.: The Indonesian Throughflow response to Indo-Pacific climate variability, Journal of Geophysical Research: Oceans, 119, 1161–1175, https://doi.org/10.1002/2013JC009533, 2014.

Sprintall, J., Wijffels, S. E., Molcard, R., and Jaya, I.: Direct estimates of the indonesian throughflow entering the indian ocean: 2004-2006, Journal of Geophysical Research: Oceans, 114, 7001, https://doi.org/10.1029/2008JC005257, 2009.

995 Sprintall, J., Gordon, A. L., Koch-Larrouy, A., Lee, T., Potemra, J. T., Pujiana, K., and Wijffels, S. E.: The Indonesian seas and their role in the coupled ocean–climate system, Nature Geoscience, 7, 487–492, https://doi.org/10.1038/ngeo2188, 2014.

Stepanek, C., Samakinwa, E., Knorr, G., and Lohmann, G.: Contribution of the coupled atmosphere–ocean–sea ice–vegetation model COS-MOS to the PlioMIP2, Climate of the Past, 16, 2275–2323, https://doi.org/10.5194/cp-16-2275-2020, 2020.

Stevens, B., Sherwood, S. C., Bony, S., and Webb, M. J.: Prospects for narrowing bounds on Earth's equilibrium climate sensitivity, Earth's
1000 Future, 4, 512–522, https://doi.org/10.1002/2016EF000376, 2016.

Sun, S. and Thompson, A. F.: Centennial Changes in the Indonesian Throughflow Connected to the Atlantic Meridional Overturning Circulation: The Ocean's Transient Conveyor Belt, Geophysical Research Letters, 47, 1–9, https://doi.org/10.1029/2020GL090615, 2020.

Tan, N., Contoux, C., Ramstein, G., Sun, Y., Dumas, C., Sepulchre, P., and Guo, Z.: Modeling a modern-like lt;igt;plt;/igt;COlt;subgt;2lt;/subgt; warm period (Marine Isotope Stage KM5c) with two versions of an Institut Pierre Simon Laplace
1005 atmosphere–ocean coupled general circulation model, Climate of the Past, 16, 1–16, https://doi.org/10.5194/cp-16-1-2020, 2020.

Tan, N., Zhang, Z. S., Guo, Z. T., Guo, C. C., Zhang, Z. J., He, Z. L., and Ramstein, G.: Recognizing the Role of Tropical Seaways in Modulating the Pacific Circulation, Geophysical Research Letters, 49, https://doi.org/10.1029/2022GL099674, 2022.

Taylor, K. E.: Summarizing multiple aspects of model performance in a single diagram, Journal of Geophysical Research: Atmospheres, 106, 7183–7192, https://doi.org/10.1029/2000JD900719, 2001.

1010 Tebaldi, C. and Knutti, R.: The use of the multi-model ensemble in probabilistic climate projections, Philosophical Transactions of the Royal Society A: Mathematical, Physical and Engineering Sciences, 365, 2053–2075, https://doi.org/10.1098/RSTA.2007.2076, 2007.

Tierney, J. E. and Tingley, M. P.: BAYSPLINE: A New Calibration for the Alkenone Paleothermometer, Paleoceanography and Paleoclimatology, 33, 281–301, https://doi.org/10.1002/2017PA003201, 2018.

Tierney, J. E., Malevich, S. B., Gray, W., Vetter, L., and Thirumalai, K.: Bayesian Calibration of the Mg/Ca Paleothermometer in Planktic
1015 Foraminifera, Paleoceanography and Paleoclimatology, 34, 2005–2030, https://doi.org/10.1029/2019PA003744, 2019a.

Tierney, J. E., Malevich, S. B., Gray, W., Vetter, L., and Thirumalai, K.: Bayesian Calibration of the Mg/Ca Paleothermometer in Planktic Foraminifera, Paleoceanography and Paleoclimatology, 34, 2005–2030, https://doi.org/10.1029/2019PA003744, 2019b.

Tillinger, D.: Physical oceanography of the present day Indonesian Throughflow, Geological Society Special Publication, 355, 267–281, https://doi.org/10.1144/SP355.13, 2011.

1020 Travouillon, K. J., Louys, J., Price, G. J., Archer, M., Hand, S. J., and Muirhead, J.: A review of the Pliocene bandicoots of Australia, and descriptions of new genus and species, Journal of Vertebrate Paleontology, 37, https://doi.org/10.1080/02724634.2017.1360894/SUPPL_FILE/UJVP_A_1360894_SM0876.PDF, 2017.

Trenberth, K. E., Fasullo, J. T., and Kiehl, J.: Earth's global energy budget, Bulletin of the American Meteorological Society, 90, 311–323, https://doi.org/10.1175/2008BAMS2634.1, 2009.

1025 Vecchi, G. A. and Soden, B. J.: Global Warming and the Weakening of the Tropical Circulation, Journal of Climate, 20, 4316–4340, https://doi.org/10.1175/JCLI4258.1, 2007.

Vecchi, G. A., Soden, B. J., Wittenberg, A. T., Held, I. M., Leetmaa, A., and Harrison, M. J.: Weakening of tropical Pacific atmospheric circulation due to anthropogenic forcing, Nature, 441, 73–76, https://doi.org/10.1038/nature04744, 2006.

Wainwright, L., Meyers, G., Wijffels, S., and Pigot, L.: Change in the Indonesian Throughflow with the climatic shift of 1976/77, Geophysical
1030 Research Letters, 35, L03 604, https://doi.org/10.1029/2007GL031911, 2008.

Wan, S., Li, A., Clift, P. D., and Jiang, H.: Development of the East Asian summer monsoon: Evidence from the sediment record in the South China Sea since 8.5 Ma, Palaeogeography, Palaeoclimatology, Palaeoecology, 241, 139–159, https://doi.org/10.1016/J.PALAEO.2006.06.013, 2006.

Wang, C.: Three-ocean interactions and climate variability: a review and perspective, Climate Dynamics, 53, 5119–5136, https://doi.org/10.1007/s00382-019-04930-x, 2019.

Wara, M. W., Ravelo, A. C., and Delaney, M. L.: Permanent El Nin˜o-Like Conditions During the Pliocene Warm Period, Science, 309, 758–761, https://doi.org/10.1126/science.1112596, 2005.

Weiffenbach, J. E., Baatsen, M. L., Dijkstra, H. A., Von Der Heydt, A. S., Abe-Ouchi, A., Brady, E. C., Chan, W. L., Chandan, D., Chandler, M. A., Contoux, C., Feng, R., Guo, C., Han, Z., Haywood, A. M., Li, Q., Li, X., Lohmann, G., Lunt, D. J., Nisancioglu, K. H., Otto-Bliesner, B. L., Peltier, W. R., Ramstein, G., Sohl, L. E., Stepanek, C., Tan, N., Tindall, J. C., Williams, C. J., Zhang, Q., and Zhang, Z.: Unraveling the mechanisms and implications of a stronger mid-Pliocene Atlantic Meridional Overturning Circulation (AMOC) in PlioMIP2, Climate of the Past, 19, 61–85, https://doi.org/10.5194/cp-19-61-2023, 2023.

Wijffels, S. and Meyers, G.: An intersection of oceanic waveguides: Variability in the Indonesian throughflow region, Journal of Physical Oceanography, 34, 1232–1253, https://doi.org/10.1175/1520-0485(2004)034<1232:AIOOWV>2.0.CO;2, 2004.

Wilks, D. S.: Statistical methods in the atmospheric sciences, vol. 16, Elsevier/Academic Press,, Amsterdam ;, 2011.

Williams, C. J. R., Sellar, A. A., Ren, X., Haywood, A. M., Hopcroft, P., Hunter, S. J., Roberts, W. H. G., Smith, R. S., Stone, E. J., Tindall, J. C., and Lunt, D. J.: Simulation of the mid-Pliocene Warm Period using HadGEM3: experimental design and results from model–model and model–data comparison, Climate of the Past, 17, 2139–2163, https://doi.org/10.5194/cp-17-2139-2021, 2021.

Wyrtki, K.: Indonesian through flow and the associated pressure gradient, Journal of Geophysical Research, 92, 12 941, https://doi.org/10.1029/JC092iC12p12941, 1987.

Yamanaka, M. D., Ogino, S.-Y., Wu, P.-M., Jun-Ichi, H., Mori, S., Matsumoto, J., and Syamsudin, F.: Maritime continent coastlines controlling Earth's climate, Progress in Earth and Planetary Science, 5, 21, https://doi.org/10.1186/s40645-018-0174-9, 2018.

Yoneyama, K. and Zhang, C.: Years of the Maritime Continent, Geophysical Research Letters, 47, https://doi.org/10.1029/2020GL087182, 2020.

Zhang, Q., Berntell, E., Axelsson, J., Chen, J., Han, Z., de Nooijer, W., Lu, Z., Li, Q., Zhang, Q., Wyser, K., and Yang, S.: Simulating the mid-Holocene, last interglacial and mid-Pliocene climate with EC-Earth3-LR, Geoscientific Model Development, 14, 1147–1169, https://doi.org/10.5194/gmd-14-1147-2021, 2021a.

Zhang, T., Yang, S., Jiang, X., and Zhao, P.: Seasonal-interannual variation and prediction of wet and dry season rainfall over the maritime continent: Roles of ENSO and monsoon circulation, Journal of Climate, 29, 3675, https://doi.org/10.1175/JCLI-D-15-0222.1, 2016.

Zhang, Y. G., Pagani, M., and Liu, Z.: A 12-Million-Year Temperature History of the Tropical Pacific Ocean, Science, 344, 84–87, https://doi.org/10.1126/science.1246172, 2014.

Zhang, Z., Li, X., Guo, C., Otterå, O. H., Nisancioglu, K. H., Tan, N., Contoux, C., Ramstein, G., Feng, R., Otto-Bliesner, B. L., Brady, E., Chandan, D., Peltier, W. R., Baatsen, M. L. J., von der Heydt, A. S., Weiffenbach, J. E., Stepanek, C., Lohmann, G., Zhang, Q., Li, Q., Chandler, M. A., Sohl, L. E., Haywood, A. M., Hunter, S. J., Tindall, J. C., Williams, C., Lunt, D. J., Chan, W.-L., and Abe-Ouchi, A.: Mid-Pliocene Atlantic Meridional Overturning Circulation simulated in PlioMIP2, Climate of the Past, 17, 529–543, https://doi.org/10.5194/cp-17-529-2021, 2021b.

Zhou, C., Zelinka, M. D., and Klein, S. A.: Impact of decadal cloud variations on the Earth's energy budget, Nature Geoscience, 9, 871–874, https://doi.org/10.1038/ngeo2828, 2016.

Zhou, C., Zelinka, M. D., Dessler, A. E., and Wang, M.: Greater committed warming after accounting for the pattern effect, Nature Climate

1070   Change, 11, 132–136, https://doi.org/10.1038/s41558-020-00955-x, 2021.
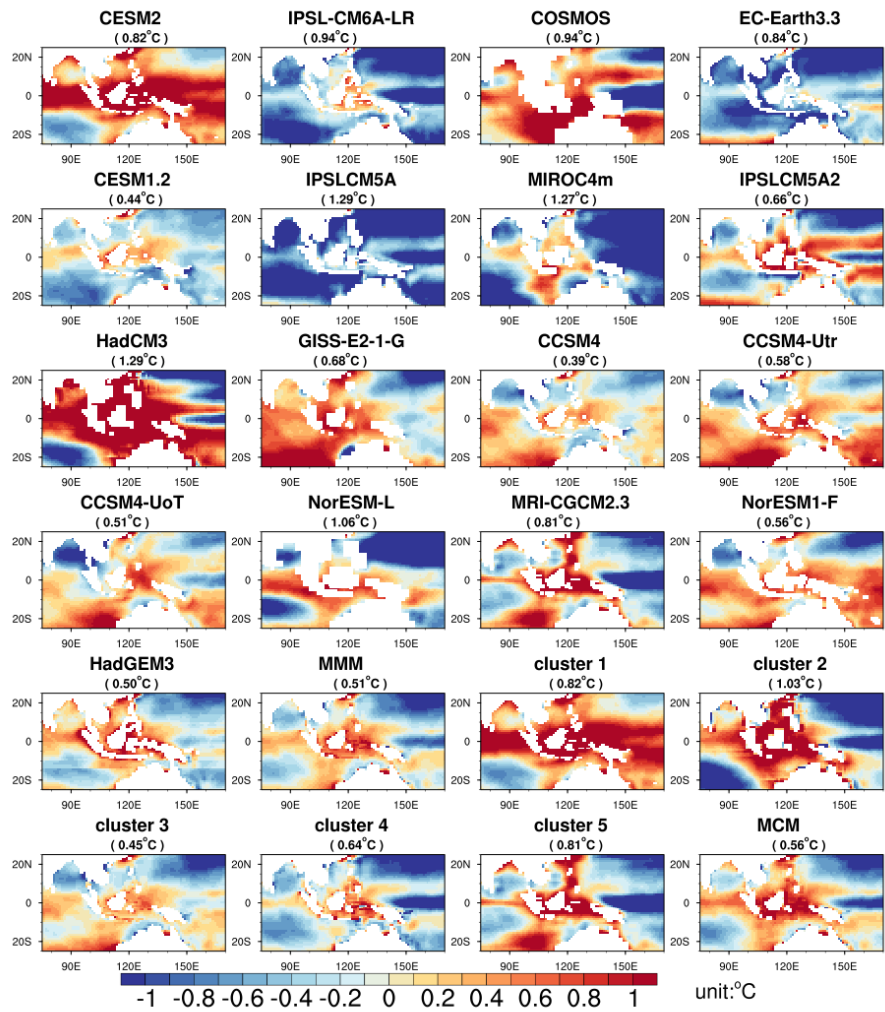
Figure S1. SST anomalies over the MC from individual models in the pre-industrial (E280) relative to HadISST1 reanalysed SSTs. Numbers in brackets indicate the RMSE between HadISST1 SSTs and model SSTs over the MC for each model.

Table S1. ~~The discrepancy values~~ Discrepancy between individual model and data. Discrepency for Eoi400 is with respect to reconstruction, for E280 with respect to HadISST reanalysis. Unit:°C

Model name	Eoi400 discrepancy	E280 discrepancy	E280 discrepancy (bias adjusted)
CESM2	2.28	0.82	0.63
IPSL-CM6A-LR	1.58	0.94	0.56
COSMOS	1.73	0.94	0.91
EC-Earth3.3	2.17	0.84	0.53
CESM1.2	1.77	0.44	0.35
IPSLCM5A	1.52	1.29	0.62
MIROC4m	1.62	1.27	0.92
IPSLCM5A2	1.58	0.66	0.65
HadCM3	1.52	1.29	1.14
GISS-E2-1-G	1.52	0.68	0.64
CCSM4	1.58	0.39	0.39
CCSM4-Utr	1.93	0.58	0.52
CCSM4-UoT	1.62	0.51	0.50
NorESM-L	1.62	1.06	0.96
MRI-CGCM2.3	1.58	0.81	0.81
NorESM1-F	1.62	0.56	0.54
HadGEM3	2.08	0.50	0.50
MMM	1.58	0.51	0.50
cluster 1	2.28	0.82	0.63
cluster 2	2.28	1.03	1.03
cluster 3	1.58	0.45	0.44
cluster 4	1.58	0.64	0.55
cluster 5	1.58	0.81	0.81
MCM	1.62	0.56	0.56
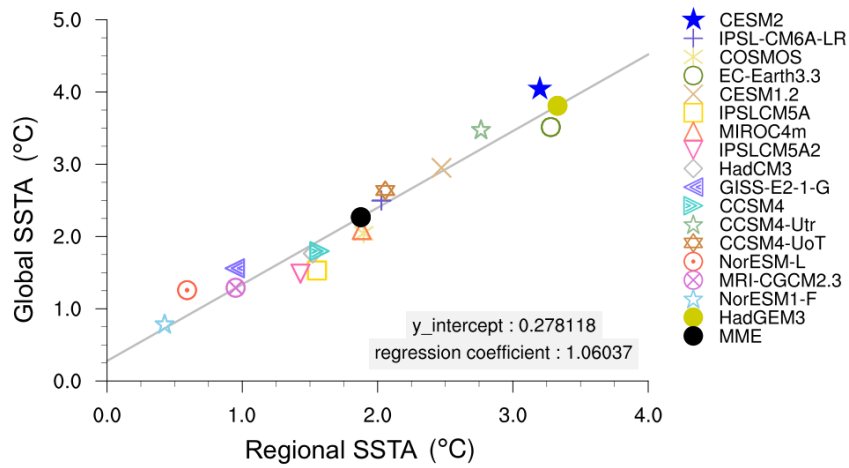
The comparison of the global SSTAs and the mean SSTAs over the MC.
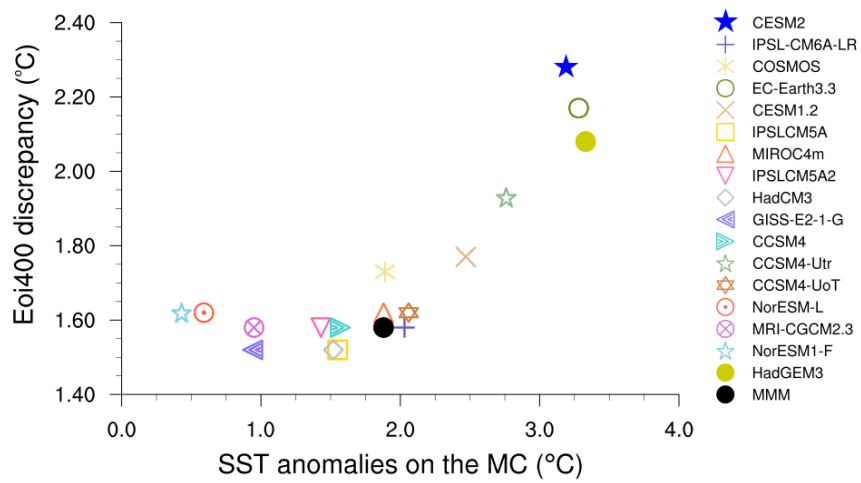
Figure S2. ~~The comparison~~ Comparison of the SSTAs averaged over the MC ~~and~~ to the Eoi400 discrepancy with proxy. Discrepancy values are as shown in Table S1.
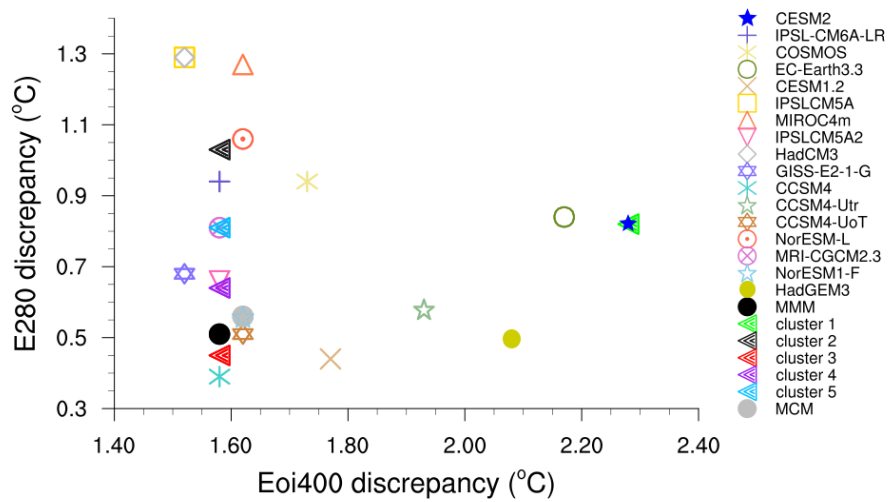
Figure S3. Comparison of the model and data discrepancies of the MC between the E280 and Eoi400 simulations. Discrepancy values are as shown in Table S1. The uncertainty of the Eoi400 discrepancies can be seen in Fig.3b of the manuscript. The unit is °C.
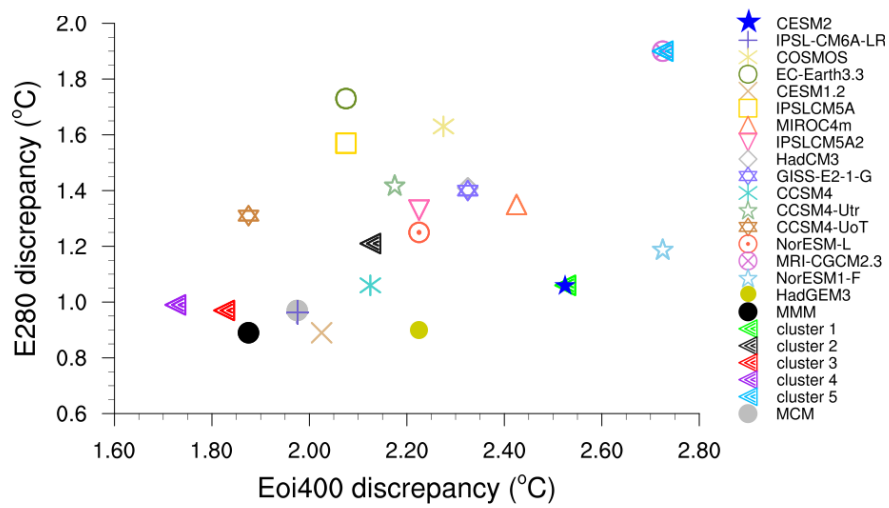
Figure S4. Comparison of ~~the~~ model and data discrepancies at the global scale between the E280 and Eoi400 simulations.
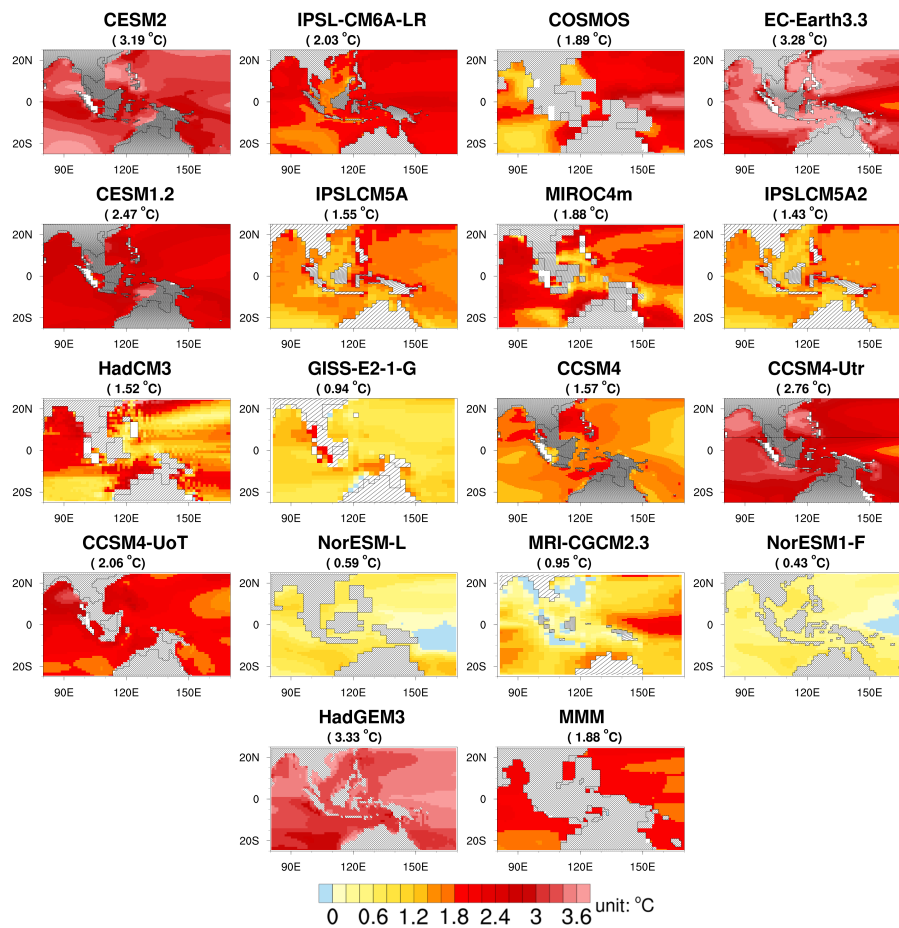
Figure S5. SSTA over the MC from individual models in the mid-Pliocene simulation (Eoi400) relative to the preindustrial simulation (E280). Numbers in brackets indicate the regional mean SST anomalies for each model.

Figure S6. ~~Same as~~ As Figure S5, but for precipitation minus evaporation (P-E).

Table S2. Proxy data in terms of wetter, drier or non-change condition used in Fig. 4b.

No.	Description	Proxy	Reference
0		paleolakes/diatomaceous sediment	Owen and Utha-aroon (1999)
1	weakened east asian monsoon; less Asian aridification	benthic and planktonic foraminiferal record; terrigenous sediment	Li et al. (2004); Wan et al. (2006)
2	less fertility of surface water, weakened East Asian winter monsoon	planktonic foraminifers δ13C	Jian et al. (2003)
3	In the late Pliocene, the climate gradually became drier, but it was substantially wetter than today.	palynofloras	Martin and McMinn (1994); Martin (2006
4	In northeastern Australia, tropical warm conditions prevailed throughout the Pliocene.	based on the evolution of both plants and animals	Archer and M (1976); Travouillon et al. (2
5	Northwestern continent was more humid during the Pliocene period	potassium, thorium and uranium, as well as common clay minerals	Christensen et al. (2017)
6	Casuarinaceae–savanna has been reconstructed for the interior implying a warmer and wetter climate than today	fossil pollen- and spore-based estimates	Macphail (1997)
7	The sedimentary characteristics of the fluvial and lacustrine sediments suggests that this was an interval of intermittent stream flow under relatively arid conditions	lake deposition	(Alley, 1998; Macphail et al., 1994)
8	ever-green rain forest was still confined to the coastal mountainous areas, with rainfall levels similar to present	NAN	Macphail (1997); Martin Helene and Andr
9	insignificant change	NAN	Macphail (1997); Martin Helene and Andr
10	insignificant change	NAN	Kershaw and Sluiter (1982)
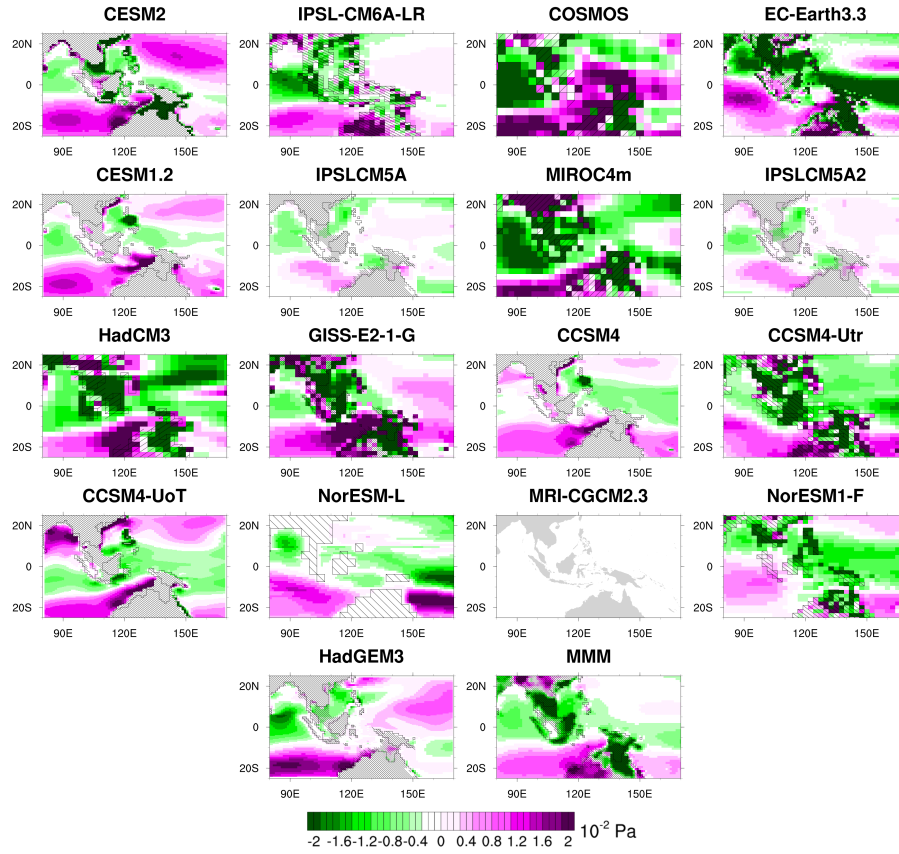
Figure S7. ~~Same as~~ As Figure S5, but for zonal wind stress. Green shading indicates westward tendency~~and~~, yellow shading indicates eastward tendency. Figure for MRI-CGCM2.3 is blank due to data availability. Unit: Pa.
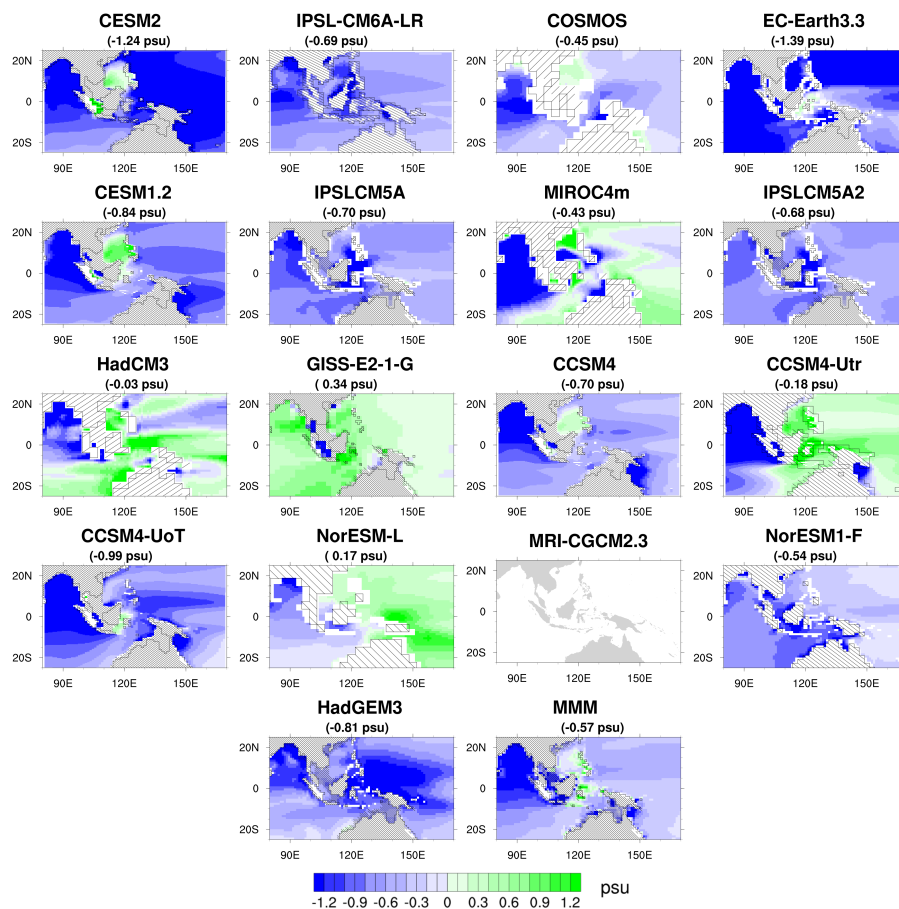
Figure S8. ~~Same as~~ As Figure S5, but for sea surface salinity (SOS). Figure for MRI-CGCM2.3 is blank due to data availability.
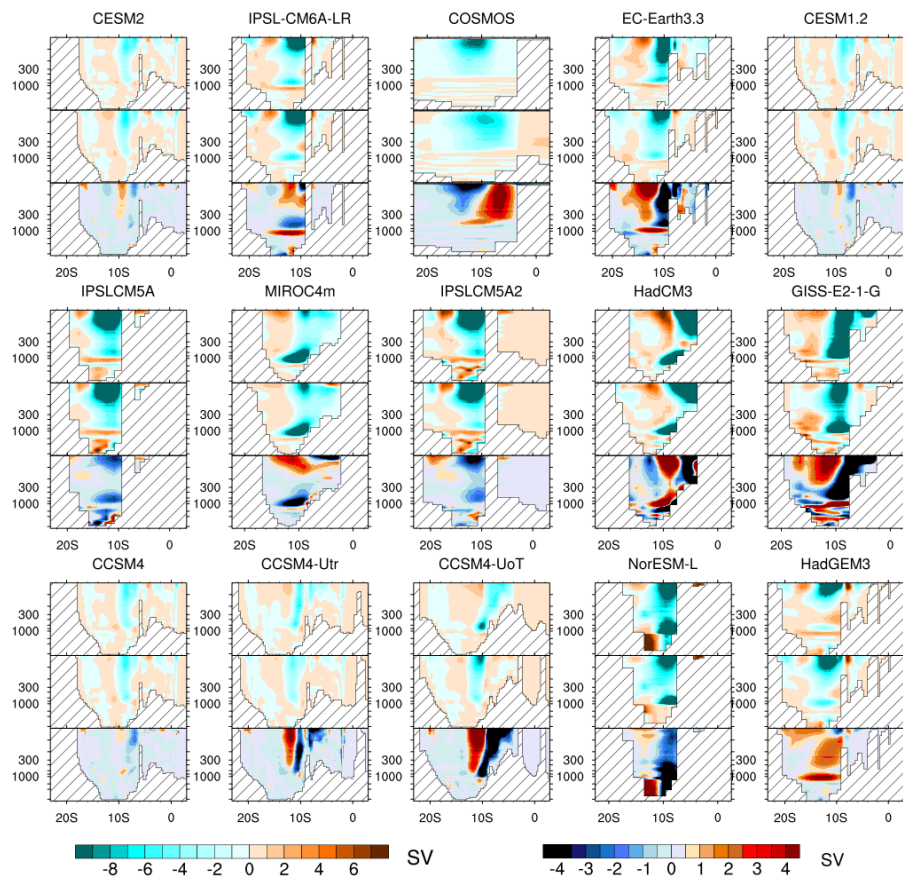
Figure S9. ~~The profiles~~ Profiles of the ~~ocean current through the MC~~ volume absolute transport of Timor strait in the mid-Pliocene (top panel for each model), in the preindustrial (middle panel for each model) and ~~the anomalies~~ anomaly of the mid-Pliocene relative to preindustrial (bottom panel for each model). Warm shading indicates direction from west to east. Cold shading indicates direction from east to west. Left color bar for absolute transport (top and middle panel), right color bar for anomaly.
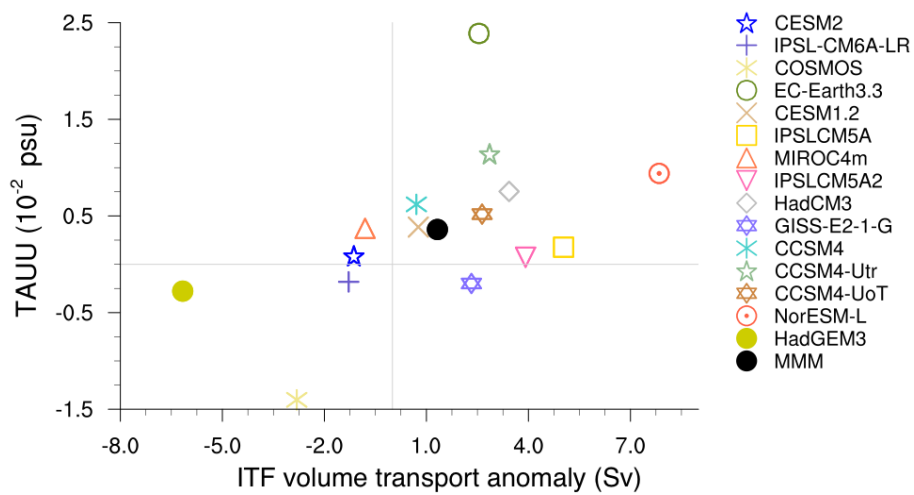
Figure S10. Comparison of the ITF volume transport anomalies and the western tropical Pacific (5S–5N, 120E–180E) zonal wind stress (TAUU) anomaly of the mid-Pliocene relative to preindustial.
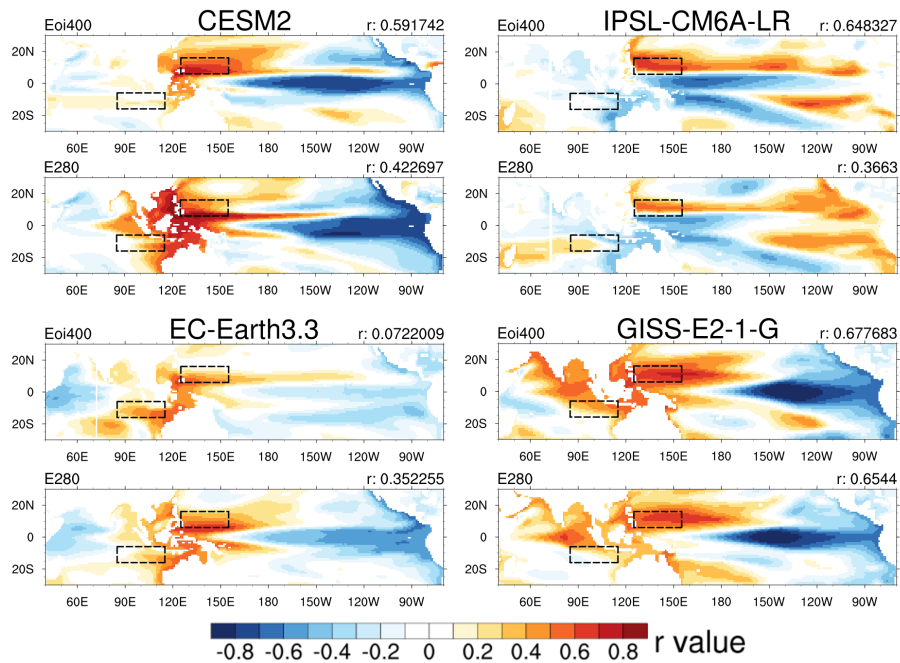
Figure S11. Map of linear regression coefficients in the annual SSH onto the annual ITF volume transport. Regions in black rectangles indicate western Pacific Ocean (6N – 16N, 125E – 155E) and eastern Indian Ocean (6S – 16S, 85E – 115E) regions for the calculation of the SSH gradient. The selection of the regions refers to Shilimkar et al. (2022). The r-value on the right top of each figure is the regression coefficient of the ITF volume transport and the SSH gradient between the western Pacific Ocean and the eastern Indian Ocean.

Figure S12. Zonal ocean volume transport intensity from individual models in the mid-Pliocene simulation (Eoi400) and the preindustrial simulation (E280). Red lines indicate transectes for the calculation of the total volume transport of the ITF.
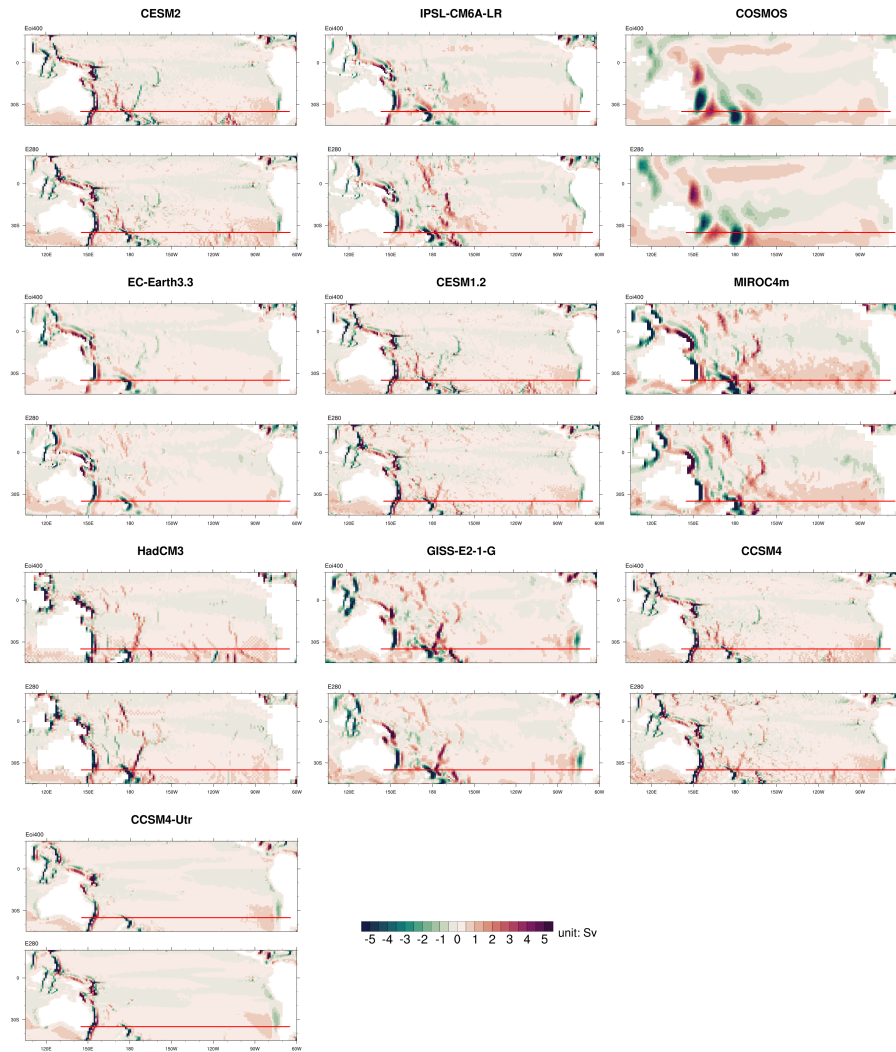
Figure S13. Meridional ocean volume transport intensity over the southern Pacific basin from individual models in the mid-Pliocene simulation (Eoi400) and the preindustrial simulation (E280). Red lines indicate transectes for the calculation of the volume transport into the Pacific basin. There are less models than Figure S12 due to data availability.
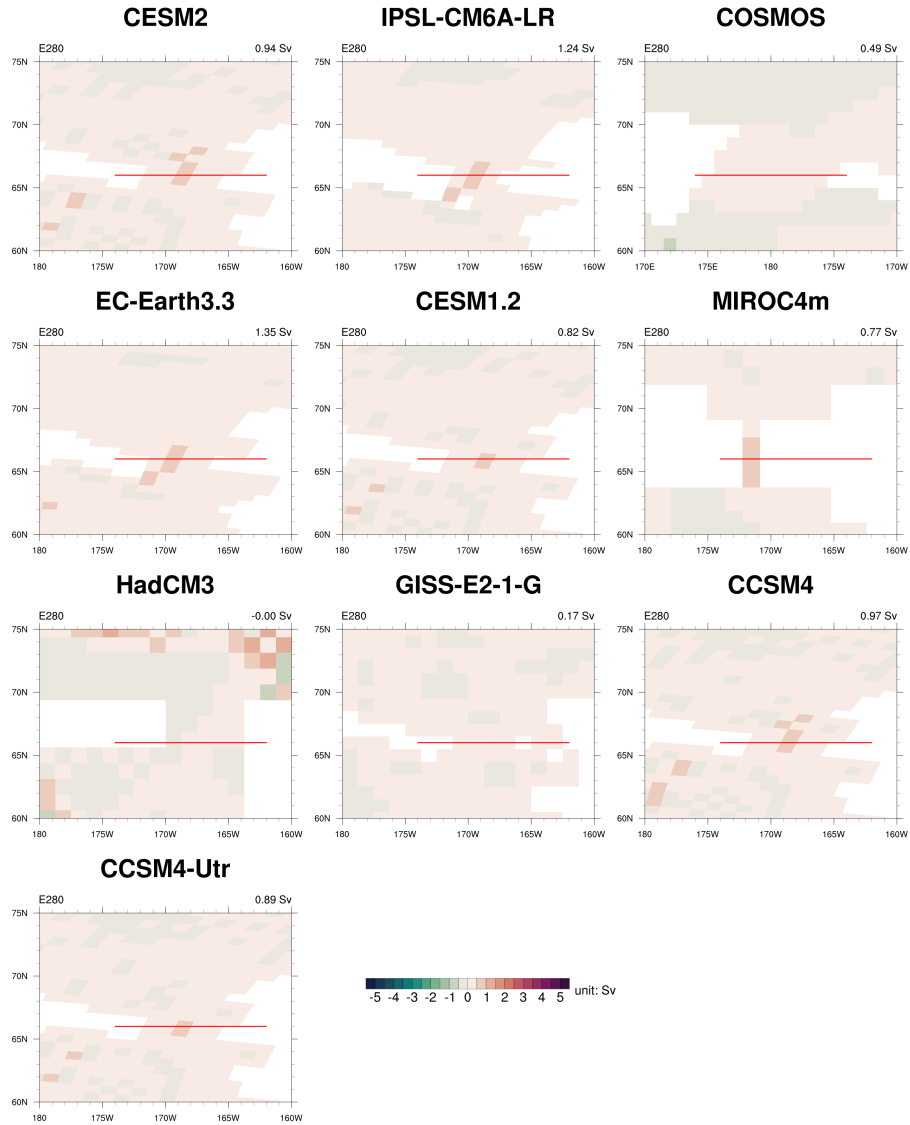
Figure S14. The meridional ocean volume transport intensity through the Bering Strait from individual models in the mid-Pliocene simulation (Eoi400) and the preindustrial simulation (E280). Red lines indicate transectes for the total volume transport of the Bering Strait. There are less models than Figure S12 due to data availability.
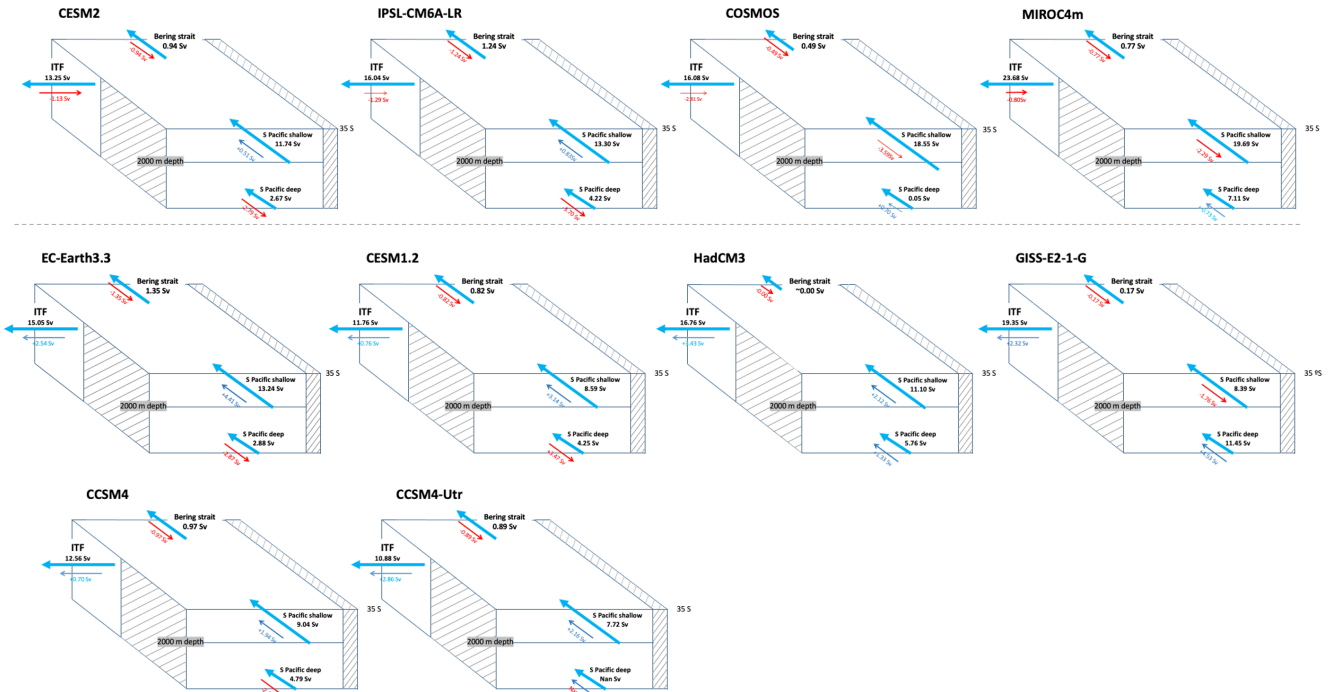
Figure S15. Basin (north of 35°S), Bering Strait and Indonesian Throughflow. The flow into the Pacific basin from the south is calculated from the shallow water above 2000 meters depth and deep water below 2000 meters depth. Blue and red for thin arrows indicate increased and decreased transport, respectively. Top panel (figures above grey dash line) shows models with decreased ITF volume transport; bottom panel (figures below grey dash line) shows models with increased ITF volume transport.